5-2012

Materials and Configuration from NMIS Type Neutron Imaging and Gamma Spectroscopy

Alicia Lauren Swift
aswift2@utk.edu

To the Graduate Council:

I am submitting herewith a thesis written by Alicia Lauren Swift entitled "Materials and Configuration from NMIS Type Neutron Imaging and Gamma Spectroscopy." I have examined the final electronic copy of this thesis for form and content and recommend that it be accepted in partial fulfillment of the requirements for the degree of Master of Science, with a major in Nuclear Engineering.

Jason P. Hayward, Major Professor

We have read this thesis and recommend its acceptance:

John T. Mihalczo, Howard L. Hall

Accepted for the Council:
Carolyn R. Hodges

Vice Provost and Dean of the Graduate School

(Original signatures are on file with official student records.)

Materials and Configuration from NMIS Type Neutron Imaging and Gamma Spectroscopy

A Thesis Presented for the
Master of Science
Degree
The University of Tennessee, Knoxville

Alicia Lauren Swift
May 2012

DEDICATION

To my parents, Robert and Linda Swift, for giving me the desire for knowledge, the curiosity for science, and the drive for success.

To my sister, Carolyn Swift, for being my best friend and biggest supporter.

ACKNOWLEDGEMENTS

I would like to acknowledge the following Oak Ridge National Laboratory and/or University of Tennessee staff:

Dr. Jason Hayward and Dr. John Mihalczo for their continued support and guidance

Dr. Brandon Grogan for his hard work generating the simulated data necessary for this project

Dr. Howard Hall for his mentorship as a committee member

Dr. Seth McConchie, Dr. James Henkel, Dr. Jim Mullens, Dr. Paul Hausladen, Dr. Eric Sword, and Mark Walker for additional help with this project

I would also like to acknowledge the US Department of Energy for supporting this work at Oak Ridge National Laboratory.

ABSTRACT

The Nuclear Material Identification System (NMIS) was first developed at Oak Ridge National Laboratory (ORNL) by the US Department of Energy (DOE) in 1984 for nuclear material control and accountability, and for possible future treaty verification applications by the Office of Nuclear Verification since the mid-1990s. NMIS is being developed into a fieldable form (designated FNMIS) and will incorporate gamma spectroscopy and an information barrier. This project, supported by the US DOE at ORNL, tested a previously developed procedure to determine the configuration of an object with unknown geometry and composition from neutron imaging, induced fission radiation detection, and passive and active gamma spectroscopy data. Using this procedure and simulated data from MCNP-PoliMi and MCNPX version 2.6.0, the problem was for one without knowledge of the object to determine its configuration and materials. Gamma spectroscopy showed that polyethylene was on the outside with depleted uranium (DU) metal inside of the polyethylene. Analysis of fast neutron imaging data determined estimates of the radii, heights of the materials, and the presence of a central void. Analysis of the fission mapping data showed that highly enriched uranium (HEU) metal was inside the DU. Since transmission imaging cannot distinguish DU from HEU metal, fission mapping was used to determine the boundary between HEU and DU. Models created from the simulated data were iterated upon by varying the enrichment of the HEU until the calculated time distribution of coincidences agreed with the simulations. The best approximation of the unknown object was concentric cylinders composed of an inner void inside of HEU (84.7 wt% ^{235}U), surrounded by DU, surrounded by polyethylene. The final estimation had the correct materials and geometry, with error in the radii estimates of material regions varying from 1.58% at best and -4.25% at worst; error in the height estimates varied from -2% to 12%. The error in the HEU enrichment estimate was 5.9 wt%, or within 2.5σ [sigma] of the true value. The accuracies of these determinations could be adequate for arms control applications. Future work will apply this iterative reconstructive procedure to other unknown objects to further test and refine it.

TABLE OF CONTENTS

LIST OF TABLES

Table Page

LIST OF FIGURES

CHAPTER I
INTRODUCTION AND GENERAL INFORMATION

The Nuclear Material Identification System (NMIS) has been under development at Oak Ridge National Laboratory (ORNL) since 1984, sponsored initially by the US Department of Energy (DOE) for nuclear material control and accountability applications and then by the Office of Nuclear Verification (ONV) in the mid-1990s for possible future treaty verification applications [Ref. 1]. As a result, it can be used in other nuclear nonproliferation applications, such as template matching for confirmation of inventories of weapons components [Ref. 2]. NMIS previously used a time-tagged californium spontaneous fission source (^{252}Cf) and most recently has employed an associated particle neutron generator with an embedded alpha detector to tag in both time and direction a portion of the emitted neutrons from the D-T reaction [Ref. 3]. A fieldable NMIS (designated FNMIS) is being developed to facilitate the future incorporation of gamma spectroscopy and an information barrier [Ref. 2].

This project, supported by the US DOE at ORNL, used Monte Carlo simulated NMIS time coincidence distributions, fast neutron imaging, fission mapping, and passive and active time-tagged gamma ray spectrometry to analyze an unknown configuration of fissile and other material, Object 1. The simulated NMIS-type neutron data was obtained with MCNP-PoliMi [Ref. 4] and the gamma ray spectrometry data was modeled with MCNPX version 2.6.0 [Ref. 5]. This simulated data were presented for analysis to the author with no knowledge of the object to determine the configuration and materials of Object 1 through a previously determined process [Ref. 6]. As such, it was a blind study to determine how much information could be obtained from each individual step in the procedure, as well as collectively. In brief, this process entailed using the provided simulated data to form an estimate of the configuration of Object 1. This estimate which was then modeled with MCNP-PoliMi, analyzed, and compared to the provided time distribution of coincidence data. If necessary, this process was repeated until convergence was achieved.

This paper is divided into 3 main sections: one which describes the NMIS measurement system, another that details the simulation methods, and a third that discusses the analysis process of the simulated data. It concludes with the best estimate of the configuration of

materials of Object 1 and recommendations for future analyses of unknown objects. The steps in the procedure are given in Appendix A.

CHAPTER II
NMIS MEASUREMENT SYSTEM

The measurement system has five main components: a D-T generator with an associated alpha detector, imaging detectors, induced fission radiation detectors, the electronics necessary to condition the timing signals, a rotation apparatus (useful for objects without symmetry, such as cuboids) and a high speed (up to 1 GHz) processor to compute the time correlation in live time.

D-T Generator

NMIS uses a portable D-T generator (Thermo-Fisher Scientific API120) that employs the reaction

$$ {}_{1}^{2}H + {}_{1}^{3}H \rightarrow {}_{0}^{1}n + {}_{2}^{4}He $$

to generate 14.1 MeV neutrons for active interrogation of an unknown object [Ref. 6, 8]. This neutron energy is desirable due to its ability to more efficiently pass through materials containing hydrogen [Ref. 2]. Approximately 4 x 10^7 neutrons per second are now produced isotropically in the present NMIS generators [Ref. 9]. This is achieved by aiming a beam composed of deuterons and tritons (less than 60 microamps) at a 5 mm diameter zirconium target embedded with tritium and deuterium atoms (Figure 1).

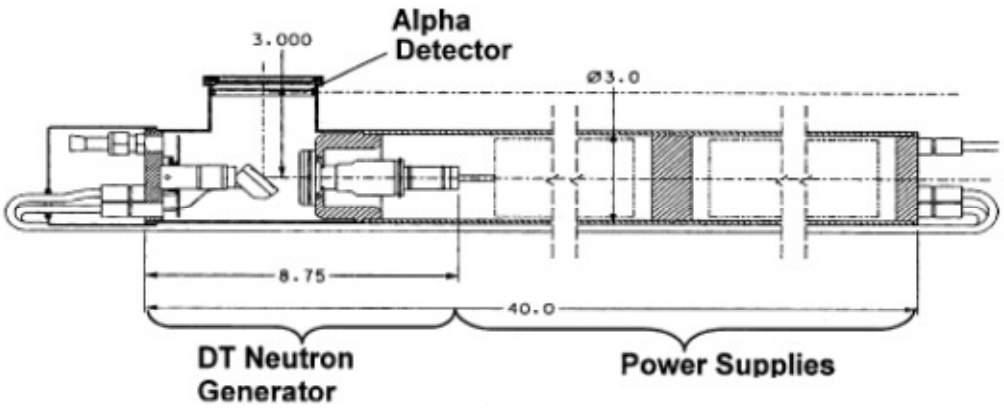

Figure 1. Diagram of the D-T generator used by NMIS for active interrogation (units are in inches) [Ref. 2].

The D-T reaction emits neutrons and 3.5 MeV alphas traveling in almost opposite directions [Ref. 1]. The generator has an associated alpha detector (a cerium-doped yttrium aluminum perovskite (YAP:Ce) scintillator) in order to define the direction of the alpha particle and thus determine the direction of the associated neutron. This process begins the radiation-generating light in the scintillator and then transfers the light through a fiber optic face plate to a Hammamatsu H9500 photomultiplier tube (PMT) on the outside of the generator. The PMT, coupled to the outside of the fiber optic faceplate, uses a row of 16 pixels to electronically collimate the neutron beam into a corresponding 16 pixel horizontal fan beam. At this point, the pixilated fan beam then passes through the interrogation object and reaches the detectors on the other side, all of which can be seen in Figure 2 [Ref. 6].

The alpha detection system serves the dual use of time- and directionally-tagging the neutrons, which is necessary for the coincidence counting used in imaging the unknown object. Because the neutron energy is known, the time of arrival of the 14.1 MeV transmitted neutrons at the detector is known, and the counts in an approximately 5 ns time window at that time are used for transmission imaging [Ref. 9]. Scattered and induced fission radiation usually arrive at the detectors at a later time.

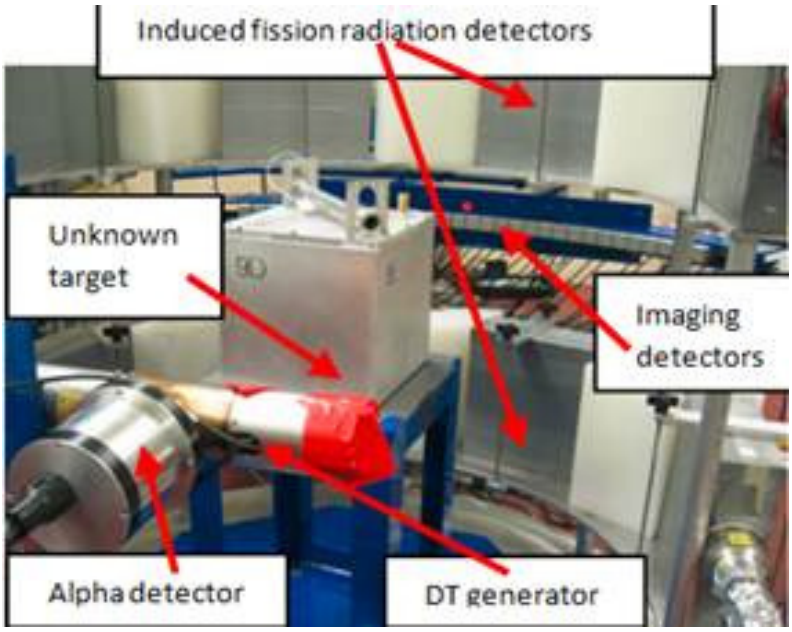

Figure 2. A labeled photograph that illustrates a typical NMIS measurement: an unknown target is interrogated by a D-T neutron generator with an associated alpha-particle detector; scattered and fission neutrons are then detected with respective imaging and induced fission radiation detectors on the far side of the object.

Imaging Detectors

NMIS now uses thirty-two 2.54 × 2.54 × 10.16 cm plastic EJ-200 scintillators as the imaging detectors, arrayed along an arc with a 115 cm radius with respect to the neutron production spot in the D-T generator [Ref. 9]. The imaging detector arc was shifted laterally in a process known as sub-sampling by some fraction of the distance between the imaging detectors, usually one-fourth of the distance between imaging detectors, in order to increase the spatial resolution and simulate a total of 128 detector positions [Ref. 7]. Coincident counts in adjacent imaging detectors within a preselected time window are not counted twice by not recording the second count that occurred.

The imaging detector arc can also be raised or lowered to perform measurements at set increments along the height (z-axis) of the object to account for the possibility of non-uniformity in its geometry or composition. Since NMIS contains a rotation mechanism on which the object is placed, the object can also be rotated at each height increment for similar reasons in the x-y plane. The data gathered at each rotation is then combined to form a sinogram, which is a plot of the detector measurement position versus the detector angular position, and from which a tomograph of the object can be reconstructed. For cylindrically symmetric objects with a vertical axis of symmetry, the rotation is not necessary if location with respect to the source is known.

Induced Fission Radiation Detectors

For these simulations and analyses, NMIS employed eight 25 × 25 × 8 cm induced fission radiation detectors that are set in a two-tier aluminum array so that four detectors sit above the imaging detectors and four sit below (Figure 2 and Figure 3). The proton recoil scintillators are separated by 6 in of polyethylene to reduce cross-talk between detectors [Ref. 10]. For this work, the fission detectors are in an arc radius of 50 cm from the center of the interrogation object [Ref. 11]. These detectors are larger than the imaging detectors to detect the induced fission radiation which is usually an order of magnitude less than the transmission radiation. These detectors are used for fission mapping and serve the purpose of measuring multiplicity, i.e. the number of single and double neutrons resulting from induced fission in the object. This information can then be used to determine the enrichment levels of fissile material

that may be present in the object because there is a direct correlation between the number of fission neutrons detected (singles, doubles, and so on) and the amount of fissile material present [Ref. 7].

To accomplish fission mapping, NMIS uses source-triggered, random and time-gated multiplicities singles, doubles, triples, etc. The time interval is selected to maximize the probability that detected neutrons are indeed from fission and are not from other sources such as inelastic gamma rays. The window begins slightly after the radiation induced by the interrogation neutrons reaches the detectors and ends when the last of the fission chain neutrons reach the induced fission radiation detectors. In theory, the gamma rays from the initial induced fissions have already passed through the detectors by the time fission neutrons arrive at the detectors. However, prompt gamma rays from fissions later in the fission chain are detected in the time window. Additional gamma ray reductions can be achieved by pulse shape discrimination with liquid scintillators; plastic scintillators can only use timing to discriminate between photons and neutrons [Ref. 7]. It is important to note that pulse shape discrimination was not used here.

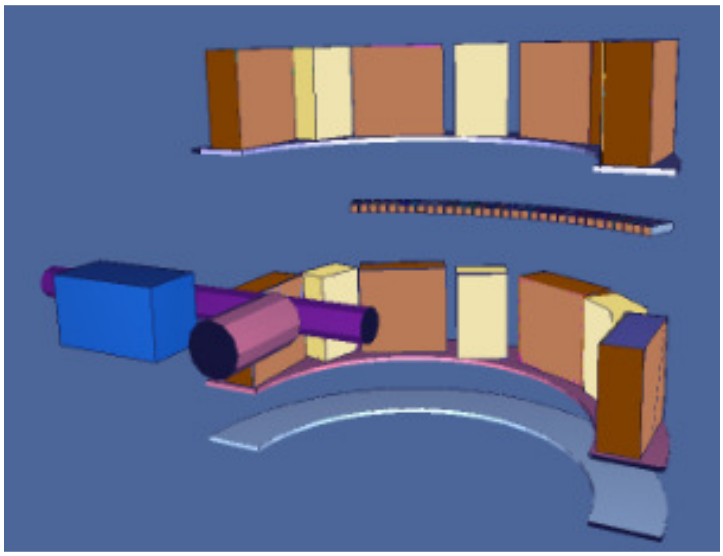

Figure 3. Diagram of the eight induced fission radiation detectors in a two-row array (dark brown) with plastic shielding (light brown) to decrease crosstalk. The thirty-two imaging detectors can be seen in the center (brown), with the D-T generator shown at left in blue and purple and its associated alpha-particle detector shown in dark pink [Ref. 7].

Electronics System and Data Processing

After digitization, all signals from all detectors go to the high speed data acquisition processor via shielded cables. The NMIS data acquisition processor computes time-correlations on-line between the 16 alpha pixels and each imaging detector in the array in 1 nanosecond increments, as well as between the induced fission radiation detectors [Ref. 1]. All correlations can be normalized to the source strength by dividing the number of counts in each time interval by the total counts recorded in that pixel over the entire measurement [Ref. 1, 12]. For an in-depth look at the capability of the processor, please see [Ref. 1]. For gamma spectroscopy, NMIS would use a multi-channel analyzer (MCA).

CHAPTER III
DESCRIPTION OF SIMULATIONS

This chapter describes the simulated data. Unless otherwise noted, it is to be assumed that the simulated data described in Chapter III was generated by Dr. Brandon Grogan of Oak Ridge National Laboratory.

Simulated Experimental Configuration

Object 1 was placed on a round stainless steel (SS304) turntable for both gamma and neutron measurements. The table had dimensions of 22.86 x 22.86 x 0.635 cm and was at a height of 56 cm above the concrete floor. Passive and active gamma spectroscopy was simulated with MCNPX version 2.6.0. The idealized simulated HPGe gamma detector was a 3" cube placed adjacent (1 mm to minimize simulation time) from the surface of the object and 90° to the central pixel of the D-T beam (Figure 4).

For neutron imaging and fission mapping, the source-to-center distance was 35 cm and the source-to-imaging-detector distance was 115 cm. Data for sixty rotations of 6° each were simulated at a height of 70 cm above the floor; this height was selected because a vertical scan of Object 1 indicated this was the height of the region of interest for a detailed internal slice, or radial tomograph. Because Object 1 was radially symmetric, only the scan obtained at a height of 70 cm was provided and the sum of all rotations was used in the analysis. In contrast, scans at multiple heights and individual rotations must be used in a measurement of an asymmetric object (for instance, a cubiod). All simulated time correlation data (specifically, transmission, scattered, and neutrons and gammas from fission) was provided by MCNP-PoliMi.

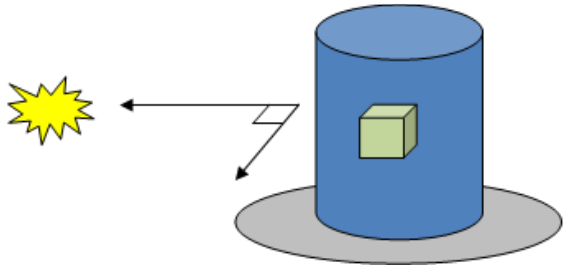

Figure 4. Illustration of the D-T source (yellow) whose center pixel is perpendicular to the HPGe detector (green). An interrogation object (blue) and table (gray) are also shown.

Simulated Gamma Spectroscopy Data

Overview of the Gamma Spectroscopy Modeling

MCNPX version 2.6.0 was used to create the passive and active gamma spectra of Object 1. Detector live time was set to 900 s for both simulations, and a normalized count was obtained via the following two step process. First, a pulse height (F8) tally in the HPGe detector was used to record the amount of energy deposited in the detector cell per particle history. Next, this value was converted to gamma counts by multiplying by the live time, the specific activity (or specific activity plus the neutron source rate if an active measurement), the total mass, and a solid angle efficiency correction. After total counts were determined, energy spreading was added to the data by assuming an energy resolution of 0.5% at the 661 keV peak and the resolution everywhere else varied from this value by the square root of the energy.

Passive Gamma Spectroscopy Data

The passive gamma ray data was obtained without an interrogation source and is a measure of the photons naturally emitted by Object 1 (e.g. radioactive decay). Physics modeling (algorithms written to model actual detector physics) was used to account for both actual energy deposition in a detector and energy broadening, resulting in features such as photopeaks, Compton edges and escape peaks. The passive spectrum is plotted as provided in Figure 5. A natural background count was not simulated since it would be subtracted in practice (and varies considerably depending on the environment) when generating the net gamma spectrum.

Active Gamma Spectroscopy Data

The active gamma ray data was simulated with an interrogation source (14.1 MeV neutrons from the D-T generator). The F8 tally had a 6 MeV cutoff energy, as well as the same physics modeling as the passive gamma data (Figure 6). The active simulation includes the passive data and that is what would be measured and subtracted in practice. Additional peaks seen in the active gamma data are a result of (n,g) and (n,n') neutron interactions in the object.

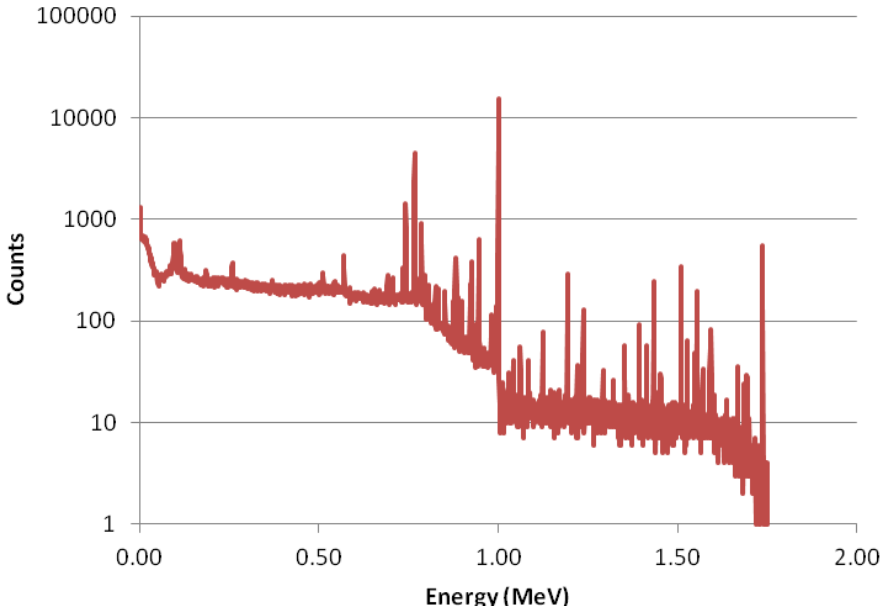

Figure 5. Passive gamma spectra of Object 1

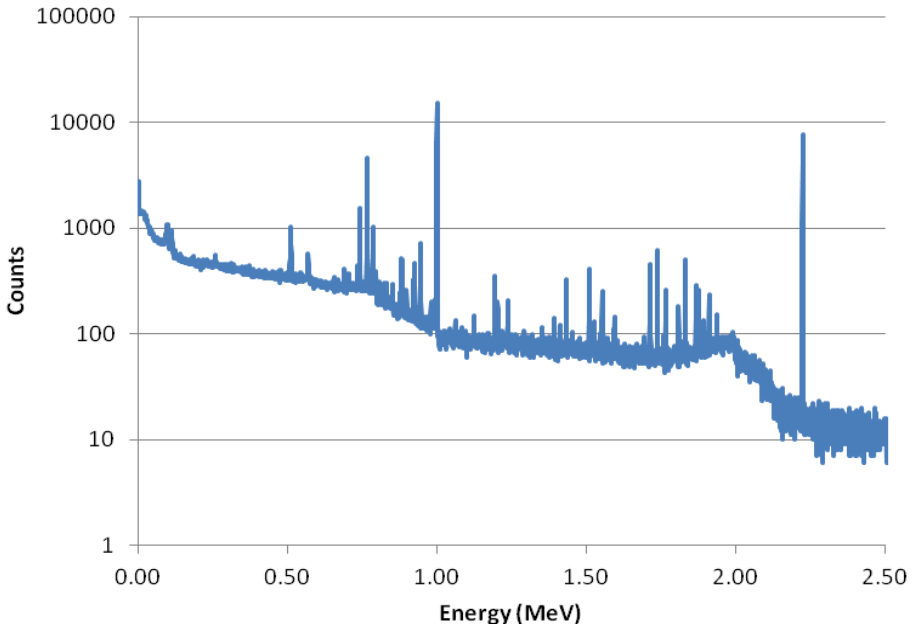

Figure 6. Active gamma spectra of Object 1

It was important to know what materials were in close proximity to Object 1 for the active simulation, as these external materials may also generate capture gamma peaks and can create false positives in the data. These external objects included the stainless steel (SS304) turntable upon which Object 1 was located, an aluminum detector measurement stand, concrete walls and floor, and lead shielding for the induced fission radiation detectors.

Simulated Neutron Imaging and Fission Site Mapping Data

Material Attenuation Theory and Transmission Imaging

Material attenuations are described by the equation below,

$$I = I_o e^{-\mu x}$$

where I is the attenuated flux of neutrons (determined with the object present), I_o is the initial flux of neutrons (determined without the object present), μ is the material-dependent attenuation coefficient for 14.1 MeV source neutrons, and x is the neutron path length (cm) [Ref. 12]. This theory is used as the basis for the two NMIS neutron image reconstruction techniques, filtered back projection (FBP) and maximum likelihood expectation maximization (MLEM) iterative reconstruction, which will be further described in coming sections. A vertical scan of the object is always completed first to determine at what height to create the detailed transmission image, a process which will be discussed in the next section. This determined that a scan be conducted at 70 cm.

Both FBP and MLEM iterative reconstruction methods that were employed to determine the configuration of Object 1 used the same data generated with MCNP-PoliMi. A void simulation was performed with no object present (I_o), followed by a simulation with the object present (I). Induced fission radiation detector simulations were run separately from transmission imaging detector simulations.

Vertical Scan Data

As stated earlier in Chapter II, a vertical scan of Object 1 was simulated by modeling the simultaneous movement of the D-T generator and detectors along the height of the object in 1 cm intervals ranging from 54 to 83 cm above the floor (Figure 7). This was necessary because

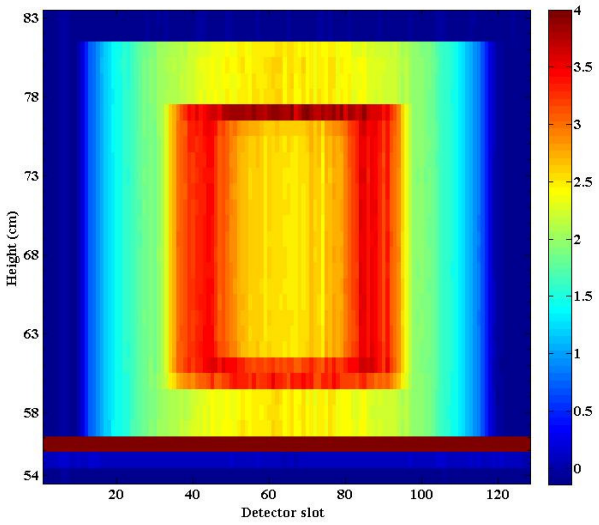

Figure 7. FBP vertical scan of Object 1 that shows the attenuation coefficient (cm^{-1}) as a function of height (cm) and detector slot. Red signifies areas of high attenuation and blue areas of low attenuation (the contrast scale measures attenuation lengths through the object).

spheres and cylinders of the same outer dimension appear the same in radial tomography in a plane at the height corresponding to the largest horizontal dimension, whereas a vertical scan easily discriminates between these two geometries. A vertical scan also determines heights of the material regions in Object 1.

Fission Mapping Data

Many reactions result from neutron interrogation, namely (n,f), (n,n'), (n,2n'), and (n,3n'). The higher the fissile mass and enrichment, the greater the amount of singles, doubles, and so on that are emitted, leak out of the assembly, and thus are available for detection. Mapping of fission sites is therefore a useful tool in determining the location, mass and enrichment of fissile material in a sample. It has been used in past measurements at Idaho National Laboratory (INL) with depleted uranium around enriched uranium to determine that the enriched uranium was on the inside. Enriched and depleted uranium have nearly the same neutron attenuations for 14.1 MeV neutrons (0.281 cm^{-1} vs. 0.279 cm^{-1}, respectively) and cannot be readily distinguished by neutron transmission, making this a useful diagnostic tool.

The eight induced fission radiation detectors used for this purpose were modeled in MCNP-PoliMi (each detector having a 50 ns dead time and an energy threshold of 1 MeV for neutrons). Each particle history was tracked for up to 256 ns.

CHAPTER IV
INTERPRETATION OF SIMULATED MEASUREMENT DATA

This section outlines the methods that were used to analyze and interpret the simulated neutron and photon data described in Chapter III to form an initial estimate of the configuration of Object 1. This estimate was then modeled with MCNP-PoliMi and compared to the reference simulation data to determine its accuracy.

Gamma Spectroscopy Data

Analysis of Passive Gamma Spectroscopy Data

Analysis of passive gamma spectroscopy data was the first step in the previously developed process of determining the configuration of Object 1. It was employed to determine what, if any, fissile or fissionable material was present. No peaks indicating the presence of weapons-grade plutonium (WGPu) were found (namely, 375 and 414 keV), but many peaks indicating the possible presence of highly enriched uranium (HEU) or depleted uranium (DU) (specifically, ^{235}U, and ^{238}U peaks) were present in the passive spectrum [Ref. 13]. Some of the visible peaks and their respective isotopes are listed in Table 1, and they are labeled on the passive spectrum in Figure 8.

Table 1. Uranium isotopes in the passive gamma spectra of Object 1

Uranium Isotope	Peak Energy (keV)
^{235}U	Low energy x-rays (95, 98, 111)
	186
^{238}U	258[1]
	511[2]
	742
	766
	786
	1001
	1193
	1510

[1] Barely visible
[2] Annihilation peak

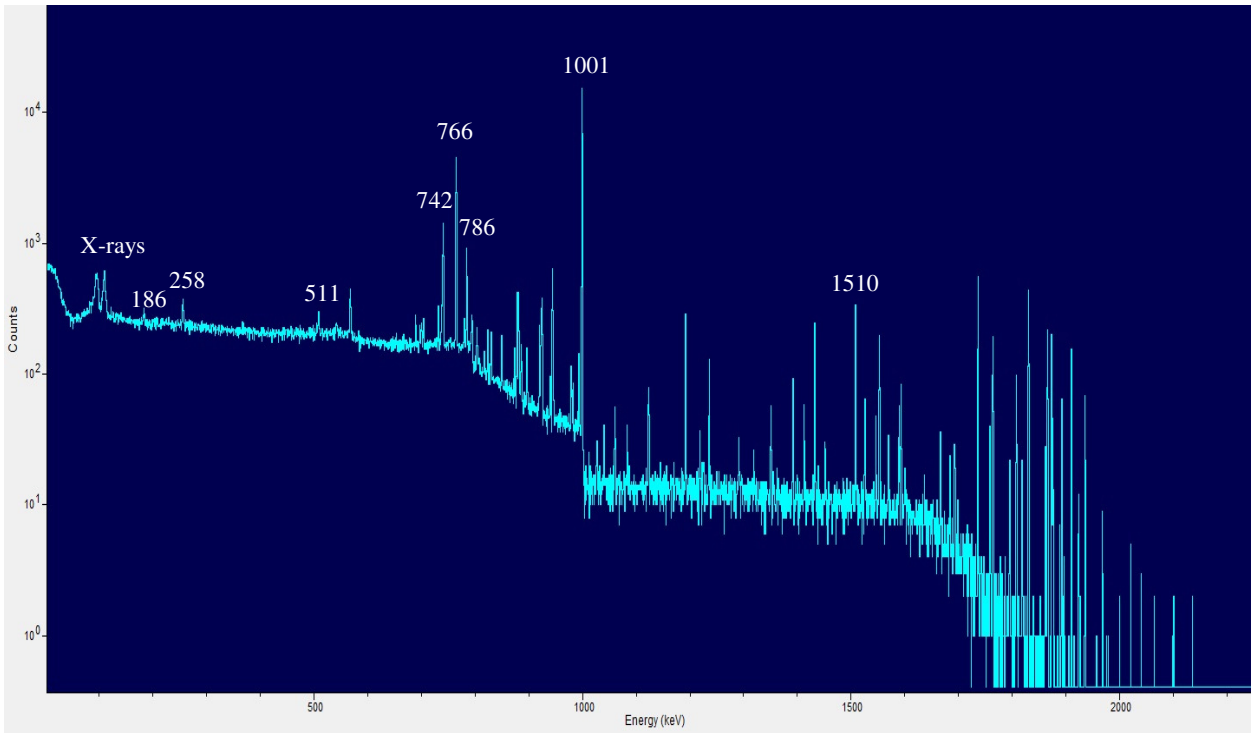

Figure 8. Significant counts in the passive gamma spectra and their energies that indicate the presence of uranium isotopes (in keV): 186, 258, 511 (pair production peak), 742, 766, 786, 1001, and 1510.

Another use for the passive gamma spectra was to determine uranium enrichment, *E*. Enrichment was estimated in two ways, the first performed by the author and the second by Dr. Brandon Grogan. The first method for estimating *E* used a ratio of the ^{235}U to ^{238}U net counts (referred to in this paper as N_{235} and N_{238}, respectively) corrected for peak yields [Ref. 12, 13]; net counts were found by selecting regions of interest. Peaks chosen for this purpose were the 186 keV (the result of ^{235}U) and 1001 keV and 258 keV (the result of ^{238}U) lines (see Appendix B and Appendix C for the equations used). By taking the ratio of peaks closer together in energy, the differing effects of attenuation previously mentioned can be mitigated and thus increase accuracy of the ratio. This is illustrated with the results, as the 186:1001 ratio yielded *E*=0.056 wt% and the 186:258 ratio yielded *E*=0.066 wt%; as the peaks get closer in energy, the enrichment approaches *E*=0.2 wt%, which is the enrichment of DU. It is important to note that HEU may be present but interior to and shielded by DU; the question of the presence of HEU will be evaluated at a later stage in the analysis process.

The second method employed GADRAS to estimate *E*. To accomplish this, GADRAS used a multiple regression iterative algorithm that "employs radiation source and detector response models to predict the response of user-defined detectors to user-defined sources" [Ref. 15]. Parameters of the geometrical model, such as materials and enrichment, were iteratively varied by GADRAS to generate an estimated spectrum to match the simulated passive spectrum. This analysis estimated *E*=0.2 wt% ^{235}U, pointing to the presence of DU with less uncertainty than the first method. This method used the total spectrum, including the low energy x-rays in the 100 keV region, which is most likely the reason for its increased accuracy because it could then account for differences in attenuation. Thus, it can be concluded from this step that DU is present.

Analysis of Active Gamma Data

Whereas the passive spectrum of the unknown object was used to determine the presence of fissile material, the active spectrum was used to ascertain the existence of non-fissile material and was the second step in forming an initial estimate of the configuration of Object 1. Significant peak energies and associated single and double escape peaks present in the active spectrum are listed in Table 2 and are labeled on the active spectrum in Figure 9. Referring to Table 2, the iron seen in the spectrum is most likely a result of (n,n') reactions from the inelastic scatter of neutrons at high energies. As such, the presence of iron in the object is doubtful.

Table 2. Nuclide peak energies for the net active gamma spectra

Nuclide	Peak Energy (keV)	Interaction Mechanism
Fe	847	(n,n')
H	1201	Double escape peak
	1712	Single escape peak
	2223	(n,g)
C	3416	Double escape peak
	3684	(n,g)
	3927	Single escape peak[1]
	4438	(n,n')[2]
	4945	(n,g)

[1] The C double escape peak from 4945 keV (E=3923 keV) could not be resolved from this (n,n') interaction
[2] The C single escape peak from 4945 keV (E=4434 keV) could not be resolved from this (n,n') interaction.

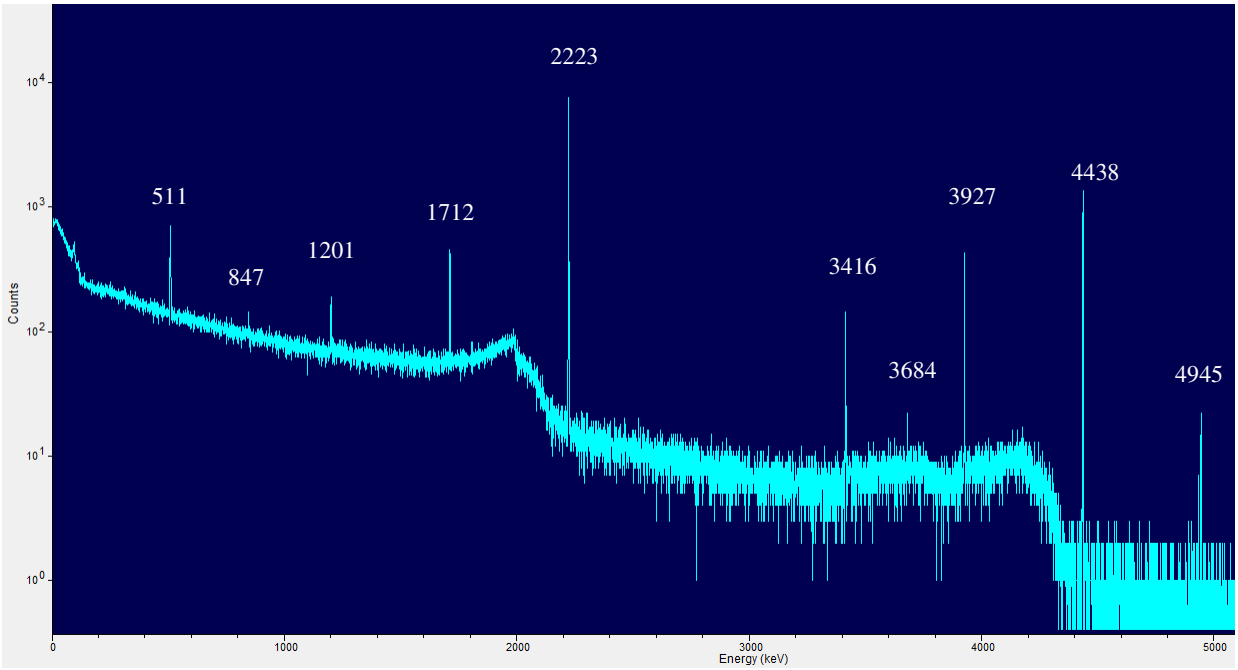

Figure 9. Significant counts in the active gamma spectra and their energies (in keV): 511 (pair production peak), 847, 1201 (double escape peak), 1712 (single escape peak), 2223, 3416 (double escape peak), 3684, 3927 (single escape peak), 4438, and 4945.

Formulation of an Initial Estimate of Materials Present in Object 1

By examining both Table 1 and Table 2, initial estimates were made on the materials comprising Object 1. These estimates, along with their corresponding material attenuation coefficients, are listed in Table 3. This was a difficult task, as some isotopes are indicators of multiple materials. For instance, carbon could be stand-alone as graphite, or it could be one of the components of polyethylene (the second being hydrogen). Thus, potential materials were initially established to be polyethylene, iron, and uranium (either in the forms of DU, HEU, or both). Iron was later ruled out due to (n,n') reactions in the stainless steel measurement table, and graphite was found to be unlikely due to the presence of the hydrogen capture gamma ray which indicates a hydrocarbon, possibly polyethylene.

Table 3. Possible materials comprising Object 1

Nuclides Found	Possible Materials	Attenuation Coefficient (x 10^{-2} cm^{-1})
C	Polyethylene	10.98
Uranium and its daughters	DU	27.90
	HEU[1]	28.14
H	Polyethylene	10.98

[1] DU might be shielding the HEU on the outside and thus HEU may be present

Transmission Neutron Imaging Data

Vertical Scan Data

Completion of a vertical scan of Object 1 was the next step after completion of the analysis of the passive and active gamma spectra. As stated earlier, this was conducted to determine regions of interest and therefore the best height to complete a radial scan of Object 1. This was chosen as the vertical center of the object, or 70 cm. This vertical scan also allowed for the determination of the height of the material regions in Object 1 (Figure 10); these heights are listed in Table 4 and were determined by Mark Walker using already developed software.

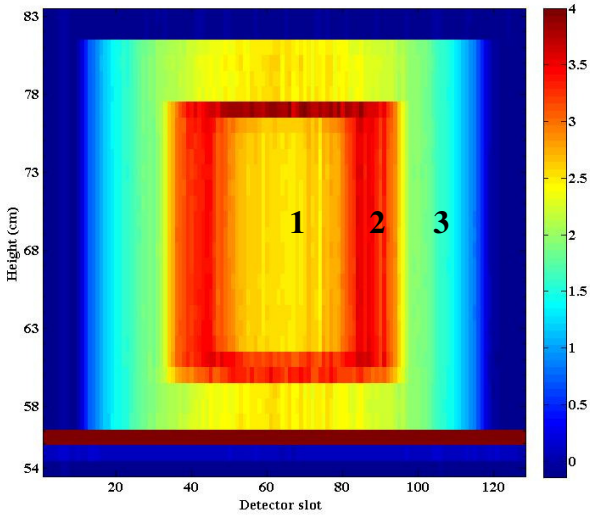

Figure 10. Vertical scan of Object 1, with red signifying areas of high attenuation and blue those of low attenuation. Supposed material regions are labeled to match those in Table 6 (regions analyzed by Mark Walker).

Table 4. Region boundaries and overall heights of the material regions of Object 1 as determined by Mark Walker

Material Region	Region Boundaries (cm)	Overall Height (cm)
1	60 to 77	17
2	59 to 78	19
3	56 to 81	25

Filtered Back Projection (FBP)

Once analysis of the passive and active gamma spectra and the vertical scan had been completed to begin to determine possible materials comprising Object 1, the next set of steps in the process dictated the analysis of the transmission neutron imaging data at the centerline. This subsequent part of the procedure allowed for the position and geometry of these materials to be established. The filtered back projection (FBP) technique was the first of two transmission image analyses that were employed for this purpose; the other technique will be described in the following section.

As previously described, the FBP method used an existing Matlab code to plot the attenuation length (μx) against detector lateral position (informally referred to as a detector slot), where each detector slot corresponds to a one of detector's four lateral subsample positions (Figure 11). The material-dependent attenuation coefficient, μ, was next isolated from μx by normalizing the attenuation length to the distance that the interaction point was within Object 1. This could be accomplished because the relative geometry of the source, detectors, and the object were all known variables, allowing for the object's dimensions (and thus x) to be determined. The attenuation coefficient was then plotted as a function of radial distance by summing all of the sixty rotations and assuming rotational symmetry, thereby forming a radial image of the material regions of Object 1 (Figure 12).

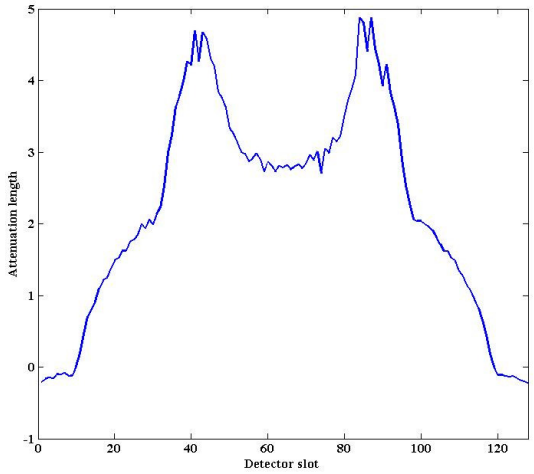

Figure 11. Attenuation lengths (μx) of Object 1 plotted against detector slot (correlates to lateral position within the object) for a single rotation.

The preceding results from the passive and active gamma spectroscopy were next used to determine the composition of the material regions visible in the FBP tomograph by matching the attenuation coefficients seen in Figure 12 with those listed in Table 3. Accounting for noise, which will be discussed in a subsequent paragraph, three material regions were therefore delineated: a central void surrounded by DU, with polyethylene comprising the outermost region (Figure 12). Although HEU may be present, its boundary cannot be determined from the FBP tomograph due to its similar attenuation value to DU, and thus at this time, only three regions are assumed; a later method will determine whether HEU is actually present.

With material regions established, the next step of the previously determined process could be completed. The boundaries of the three regions labeled in Figure 12 were approximated by visual inspection of the tomograph and then entered into a previously-written Matlab code, TAKE. These visual inspection values, along with attenuation values for the material regions, were then used as initial guesses to iterate between the measured attenuation length curve in Figure 11 and one that is produced by forward-projecting the guessed object dimensions onto the detectors (Figure 13). The purpose of running this iterative code is to estimate the dimensions of Object 1. The resultant TAKE estimates of the dimensions of these three regions are listed in Table 5.

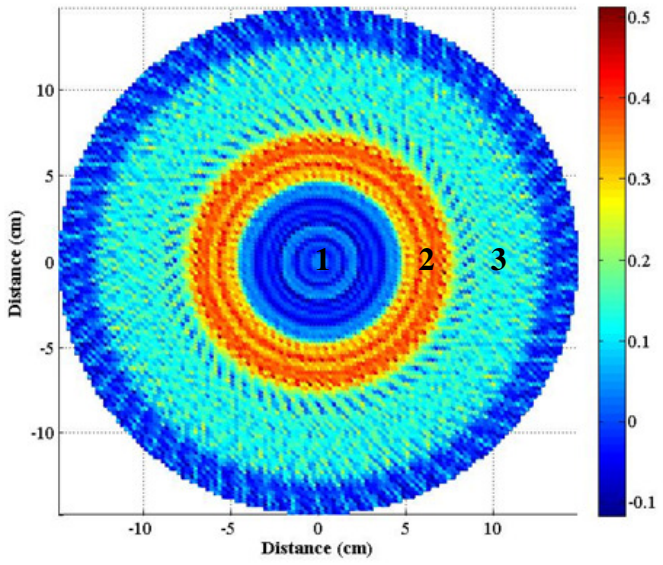

Figure 12. FBP radial tomograph of Object 1 that plots the attenuation coefficient (cm^{-1}) as a function of distance (cm). Red signifies a high attenuation and blue a low attenuation, as shown in the color bar to the right of the image. The three material regions of Object 1 are as follows: (1) void, (2) DU (possibly containing HEU on the interior), and (3) polyethylene.

It should be noted at this point that there is noise within the FBP tomograph as a result of the filtering process. For example, between -4 and +4 cm in Figure 12, it appears there are multiple thin rings of some low-attenuating material. However, it is apparent that some of these rings have negative attenuation coefficient values, which is unphysical. Additionally, the noise causes some of the attenuation values to be much higher than they normally would (most fissile materials and the materials used to shield them have attenuations below 0.3 cm^{-1}). These problems are statistical and will be addressed with the second neutron imaging technique addressed in the following section.

A final result can be drawn from the FBP transmission image when combined with the vertical scan image data collected in the previous step. The vertical and radial images lead to the conclusion that Object 1 is cylindrical.

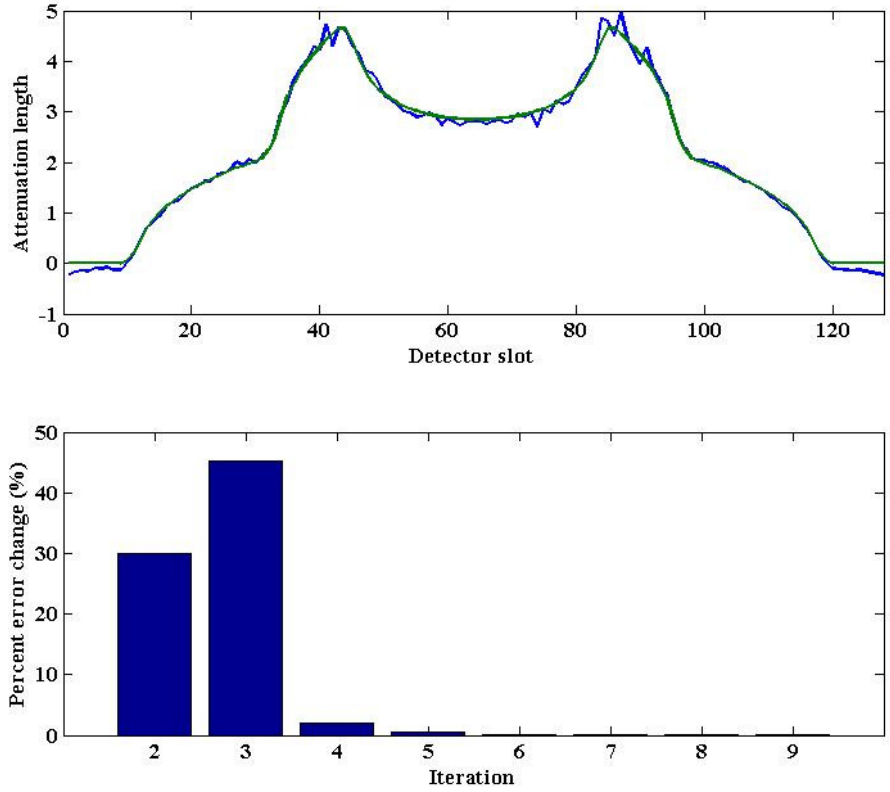

Figure 13. Top: The TAKE process iterated between the measured attenuation length curve (blue) and one that is produced by forward-projecting the guessed object dimensions onto the detectors (green). Both are for a single rotation. Bottom: Percent error change as a function of number of iterations showing convergence between the two attenuation length curves.

Table 5. TAKE radial dimensions and attenuation coefficients for Object 1

Material Region	Visual Inspection Radius (cm)	Visual Inspection μ (x 10^{-2} cm^{-1})	TAKE Radius (cm)	TAKE μ (x 10^{-2} cm^{-1})
1	4.5	0.00	4.609	0.00
2	7.7	27.90	7.500	30.84
3	12.5	10.98	12.352	10.89[1]

[1] This attenuation coefficient is consistent with polyetheylene

Maximum Likelihood Expectation Maximization (MLEM) Transmission Reconstruction

Maximum Likelihood Expectation Maximization (MLEM) iterative reconstruction was the second method used to form a transmission image of Object 1 from the simulated data. MLEM iterative reconstruction is a different process from FBP imaging in that it begins with an initial guess of 1 for the attenuation coefficient of each pixel in the reconstruction. The attenuation length (μx) for each pixel is then forward projected to create a sinogram. The ratio of the current to the previous projection is then used as a correction factor that is applied to each pixel [Ref. 9]. This process was iterated fifty times to generate a final sinogram and then a final transmission image. The initial and final guess sinograms are shown below in Figure 14, with the reconstructed sinogram on the right appearing much smoother than the original. Images of the tomographs at iteration 1, 5, and 20, along with the final reconstructed tomograph at iteration 50, can be seen in Figure 15.

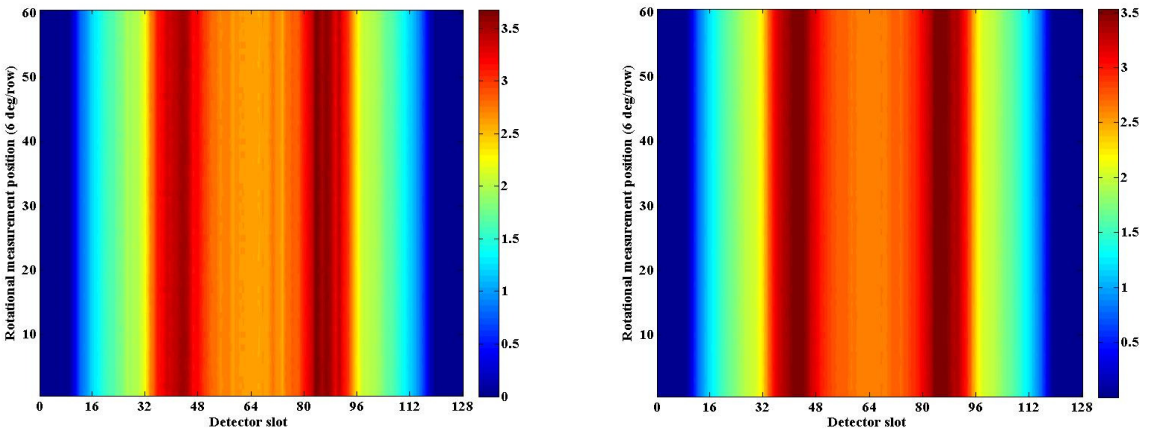

Figure 14. Initial sinogram (left) and the reconstructed sinogram (right) used to create the MLEM tomograph of Object 1. Areas in red have a high attenuation and areas in blue have a low attenuation.

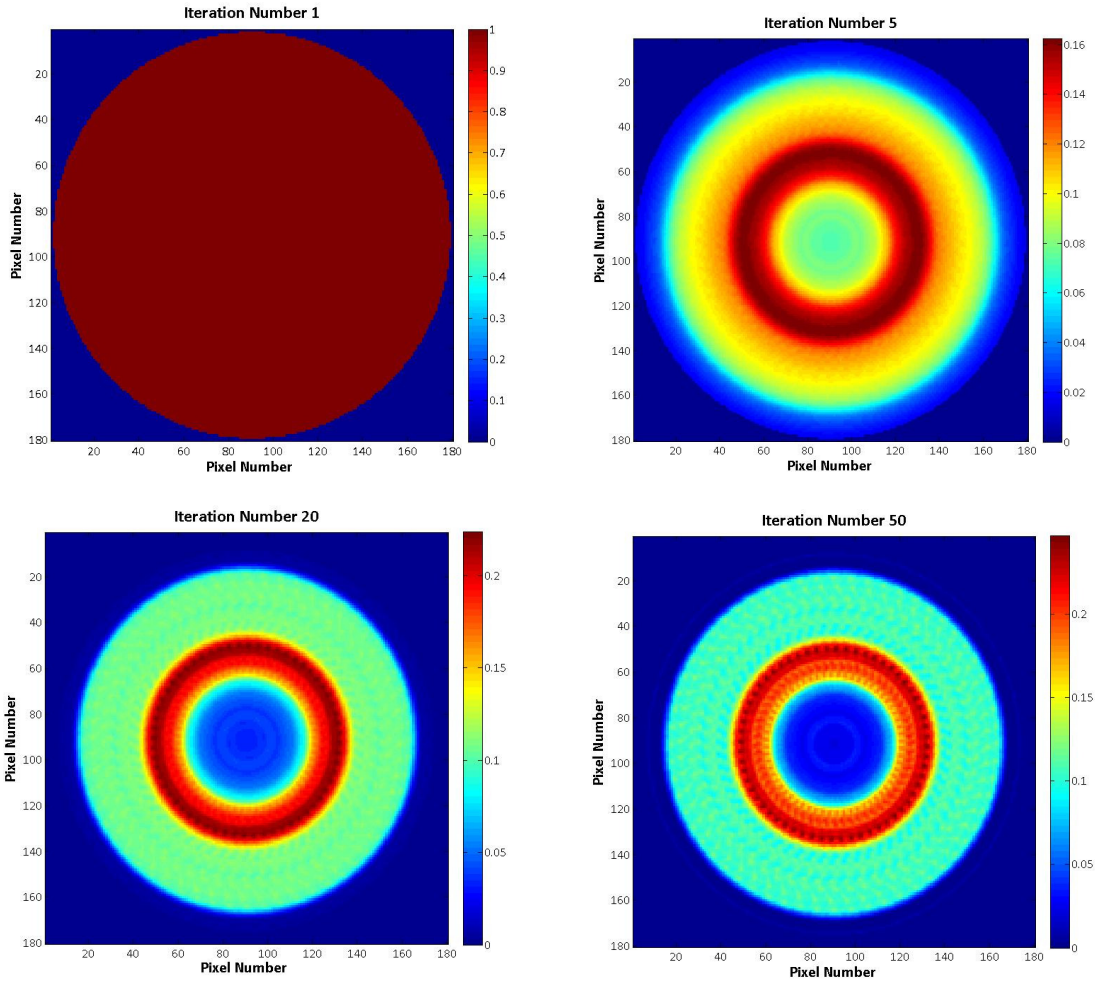

Figure 15. Reconstructed tomographs at one, five, twenty, and fifty iterations for Object 1. Areas in red have a high attenuation, and areas in blue have a low attenuation, as shown in the color bar to the right of the images. Attenuation is shown with units of cm^{-1}.

It should be noted that the MLEM reconstructed tomograph at iteration 50 has fewer artifacts than the FBP tomograph, and therefore material regions and their attenuation values are much easier to identify (Figure 16). To determine whether HEU is present and being shielded by DU, it is also necessary to complete MLEM iterative reconstruction of fission sites, a step in the procedure that will be discussed later in this section. However, one cannot rely solely upon the MLEM iterative reconstruction; the FBP method is also necessary to determine the overall dimensions of the object because the FBP method is required to run the TAKE software; therefore, both methods complement each other.

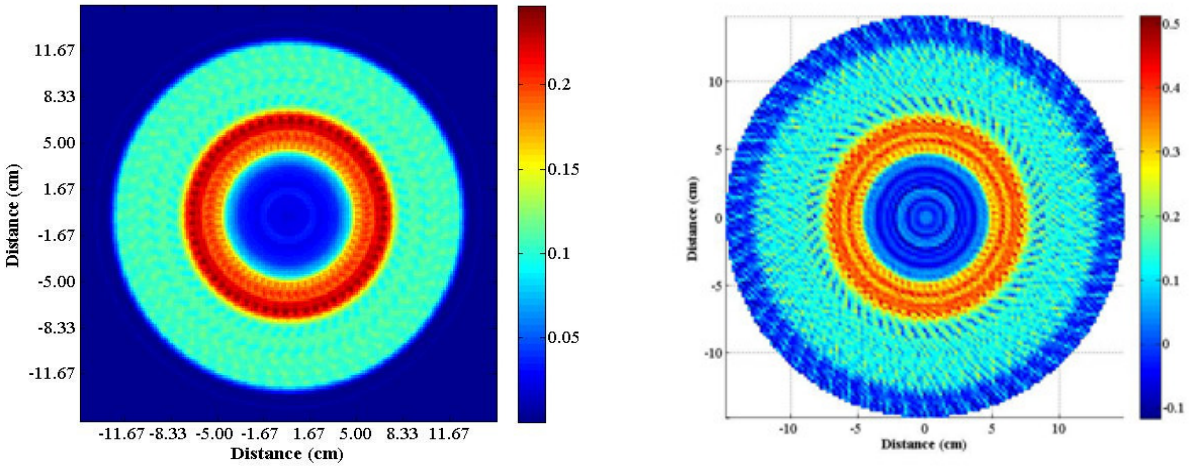

Figure 16. MLEM tomograph (left) of Object 1 at iteration 50 with adjusted x and y dimensions to show boundary positions. The tomograph from the FBP method (right) is shown here for comparison.

Fission Mapping Data

The next step in the procedure was to analyze the fission mapping data. Single and double coincidence counts that had been obtained with the induced fission radiation detectors were correlated with the alpha pixels. The data were plotted against alpha pixel number to determine how the induced fissions varied with alpha detector pixel. Fission mapping reconstructs where fission sites are located by correlating the fission neutrons measured with the alpha pixel event in order to obtain the spatial distribution of fission sites. These fission mapping (FM) plots were generated by a Matlab code and are useful for determining multiplication because their shape is dependent solely upon the object's geometry and material composition. The standard deviation, following a Gaussian approximation, was taken to be the square root of the number of simulated counts. A general rule of thumb was that the higher number of counts, and especially the number of doubles counts, the higher the multiplication at that location in the system. The distribution of doubles, plotted in Figure 17, showed that alpha pixels 5 through 12 define neutrons that impinge on the HEU.

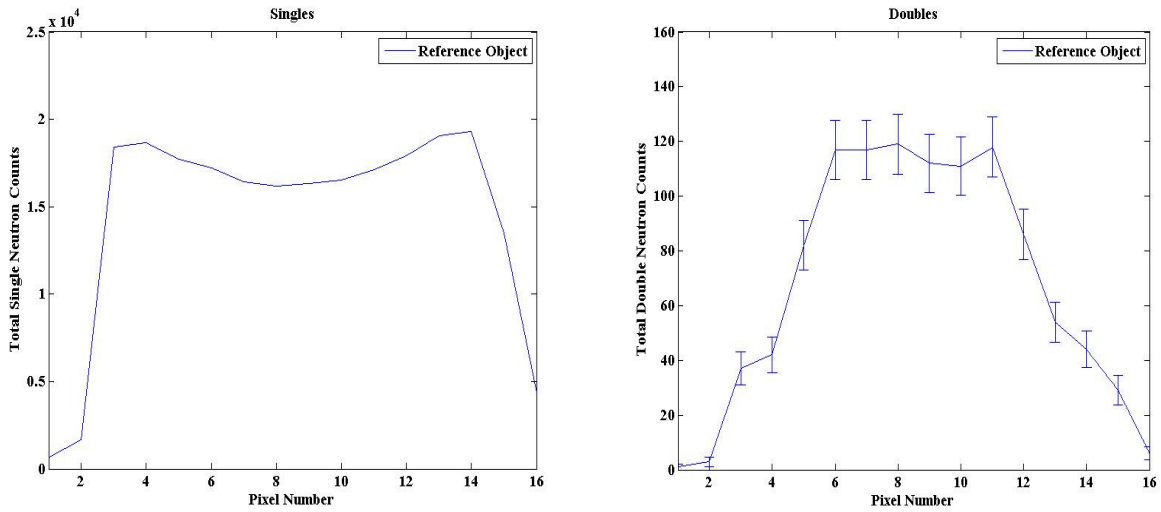

Figure 17. Fission mapping plots for single (left) and double (right) coincidence counts for the reference data. Pixels 5 through 12 see the most multiplication from the system. Error was taken to be the square root of the counts.

Multiplicities and Feynman Variances

As further verification that pixels 5 through 12 were proper choices, the Feynman variance (Y) of the single (y_1) and double (y_2) fission neutron reference data was calculated and plotted against its corresponding alpha pixel [Ref. 16, 17]. By taking the ratio of doubles to singles counts, the multiplication of the reference data that is seen by each pixel can be determined. The Feynman variance was found according to

$$Y(T) = 2\left(\frac{y_2}{y_1}\right) = 2\left(\frac{\binom{2}{2}b_2+\binom{3}{2}b_3}{\binom{1}{1}b_1+\binom{2}{1}b_2+\binom{3}{1}b_3}\right) = 2\left(\frac{b_2+3b_3}{b_1+2b_2+3b_3}\right)$$

where b_1 is the number of singles, b_2 is the number of doubles, b_3 is the number of triples, and T is the gate window width. A full derivation of this equation (which assumes signal-triggered gating) can be found in Appendix D. As can be seen in Figure 18, pixels 5 through 12 are seeing the multiplication of the system, and thus discarding the others was a proper choice.

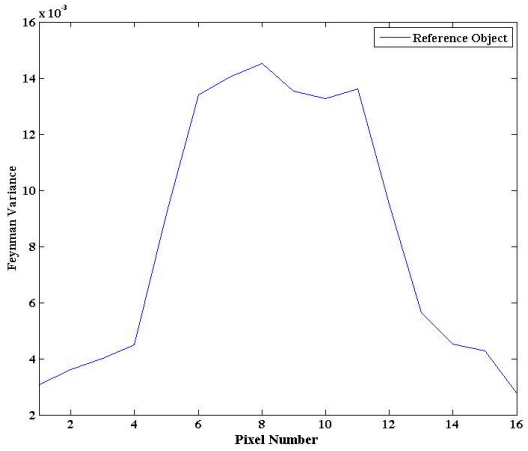

Figure 18. Feynman variance of the reference data plotted against the alpha pixel number to allow for a visualization of the multiplication seen by each pixel. Here it is obvious that pixels 5 though 12 see the most multiplication, and the outer pixels see little to none.

Maximum Likelihood Expectation Maximization (MLEM) Fission Reconstruction

The next step was to utilize the MLEM fission reconstruction methodology. Similar to MLEM transmission reconstruction, this code generates MLEM sinograms and tomographs of the single and double fission neutron sites (Figure 19 and Figure 20, respectively) and then overlays them in color on a black and white version of the MLEM transmission tomograph, previously shown in Figure 16. The color scale of the MLEM singles and doubles sinograms represents the number of singles (or doubles) detected per alpha particle and that of the singles and doubles images represents the number of singles (or doubles) detected per pixel. Fifty iterations were similarly conducted in this step.

As can be seen in the doubles overlay in Figure 21, there is a region of medium and high (colored yellow and red) fission sites, surrounded on the outside by a region of low (colored white) fission sites. These images therefore show that initial indications were correct. DU has very few fissions at 0.2 wt% ^{235}U and would therefore be white in such an image; HEU has many fissions and would be colored red. Thus, Object 1 does indeed have a region of HEU surrounded on the outside by a dense region of DU. It is important to note that the doubles data provides more insight into the fissile geometry than the singles data, and that the singles MLEM fission reconstruction results contain less insight into the region of the fissile geometry due to neutron scatter.

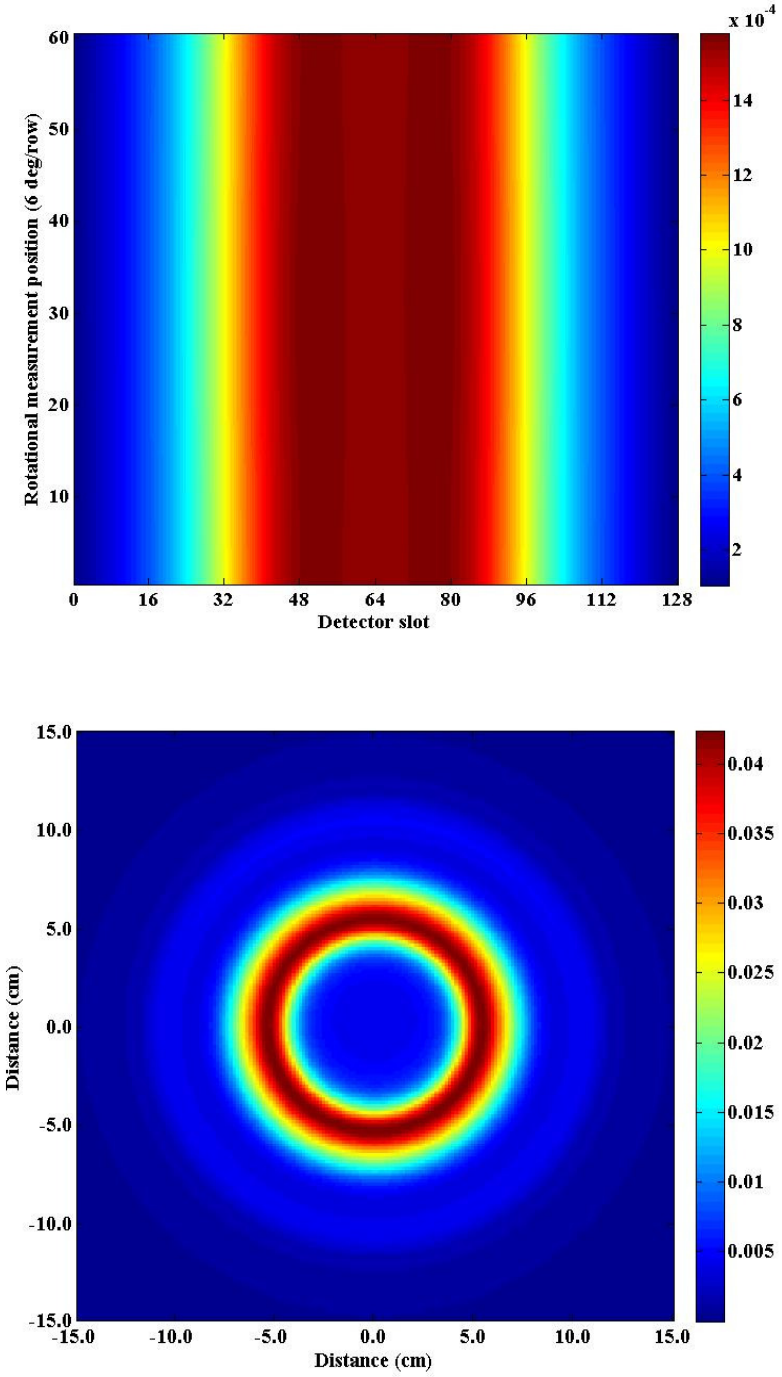

Figure 19. Singles MLEM reconstruction of the object's sinogram (top) and tomograph (bottom) after 50 iterations.

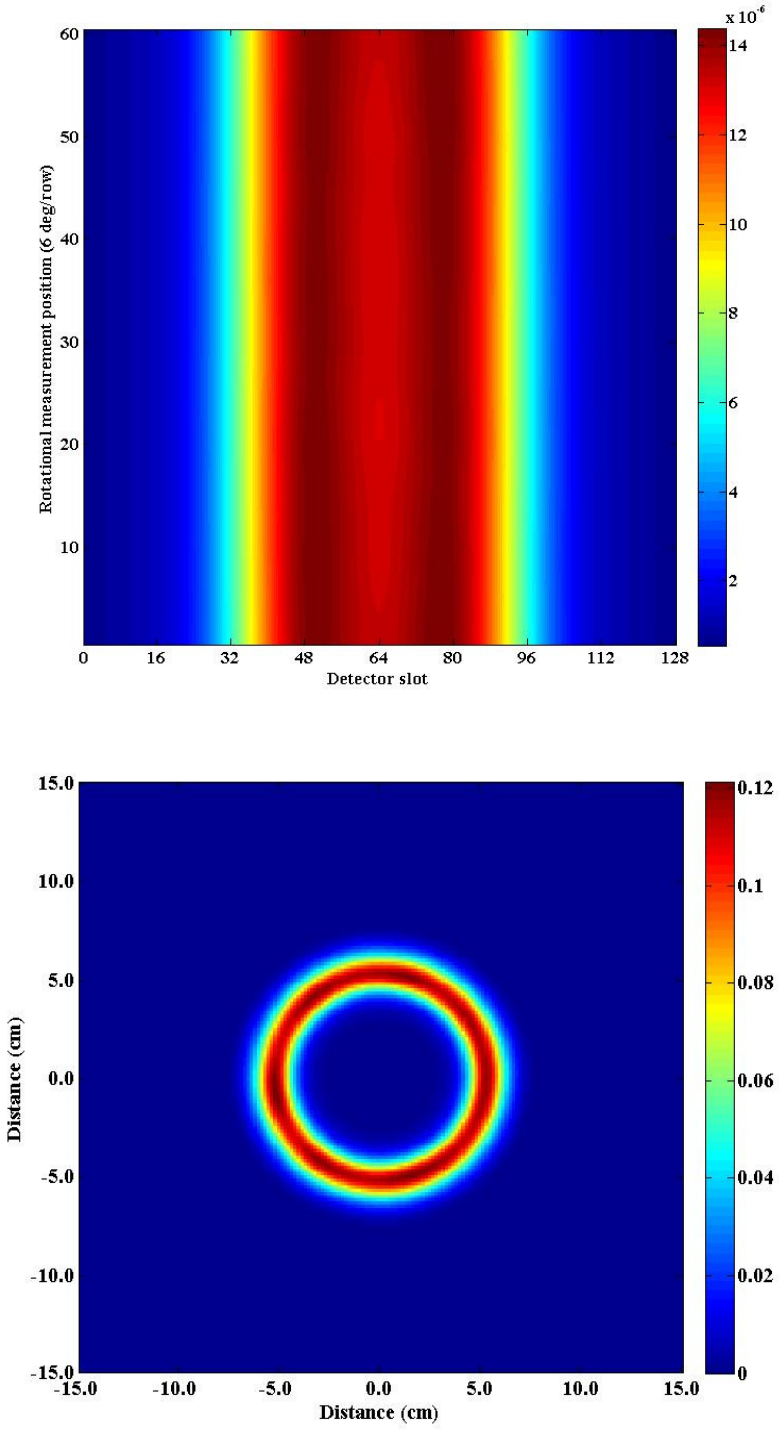

Figure 20. Doubles MLEM reconstruction of the object's sinogram (top) and tomograph (bottom) after 50 iterations.

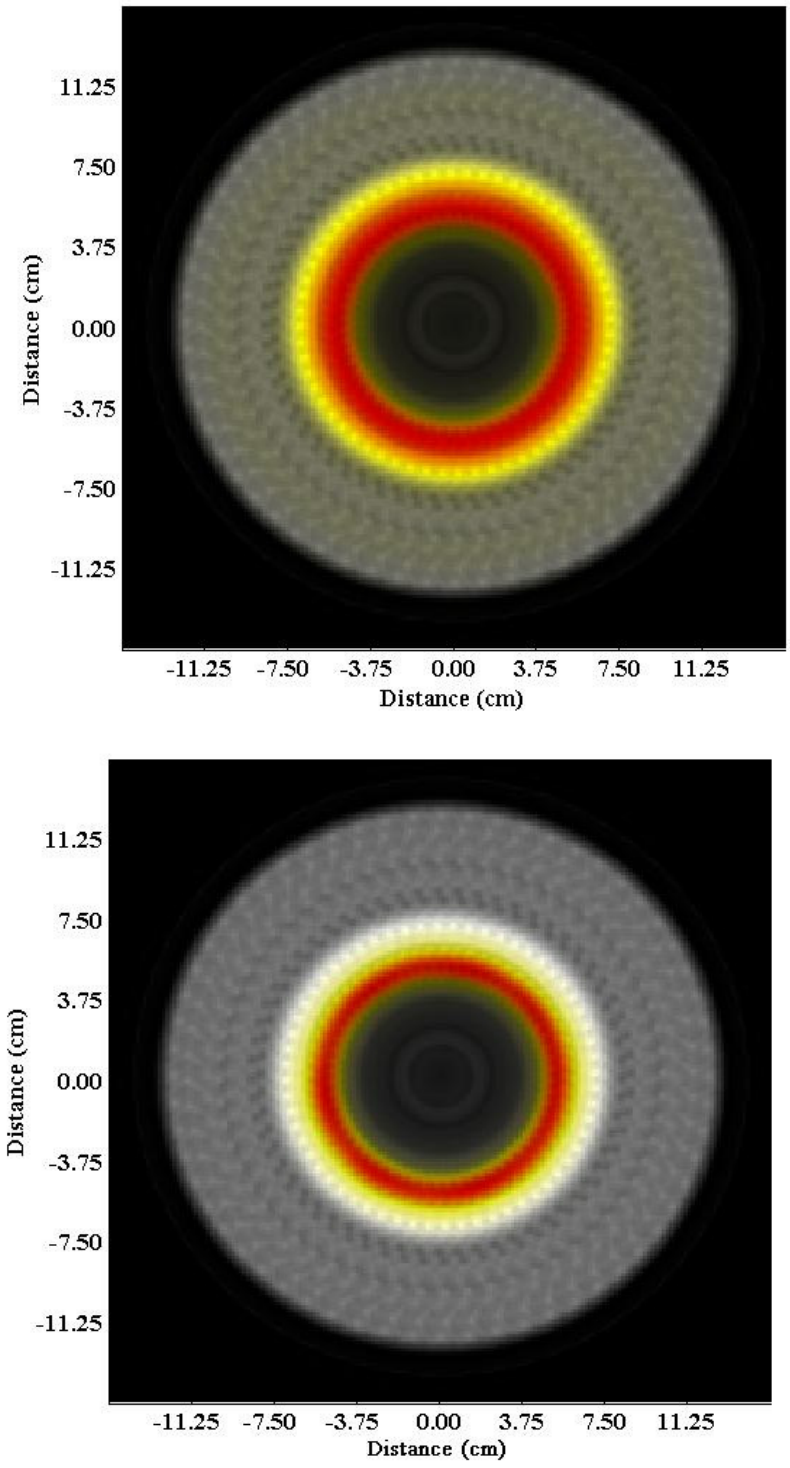

Figure 21. Overlay of the MLEM tomograph reconstruction for singles (top) and doubles (bottom) coincidence data. Red indicates high values, yellow mid values, and white low values of fission sites.

Once it was determined that there was HEU and DU present, the doubles tomograph in Figure 20 was used to determine the boundary between these two material regions. The FBP and MLEM transmission images could not be used for this purpose because of the similar attenuation coefficients of DU and HEU, and thus to determine the outer radius of HEU, the outer radius of the doubles tomograph was examined as follows. A slice of the doubles tomograph was taken at the centerline (i.e. slot 90) which formed a plot of doubles counts against detector slot (Figure 22). The radius was then approximated to be halfway between the maximum amount of doubles (corresponding to HEU) and near zero doubles (corresponding to DU), as this approximated the location of slope change. Due to the fact that HEU formed a cylinder, there were two such locations on the abscissa (54 and 127); converting these into cm (through dividing by 6) and then averaging the two together yielded an outer radius of HEU of 6.08 cm.

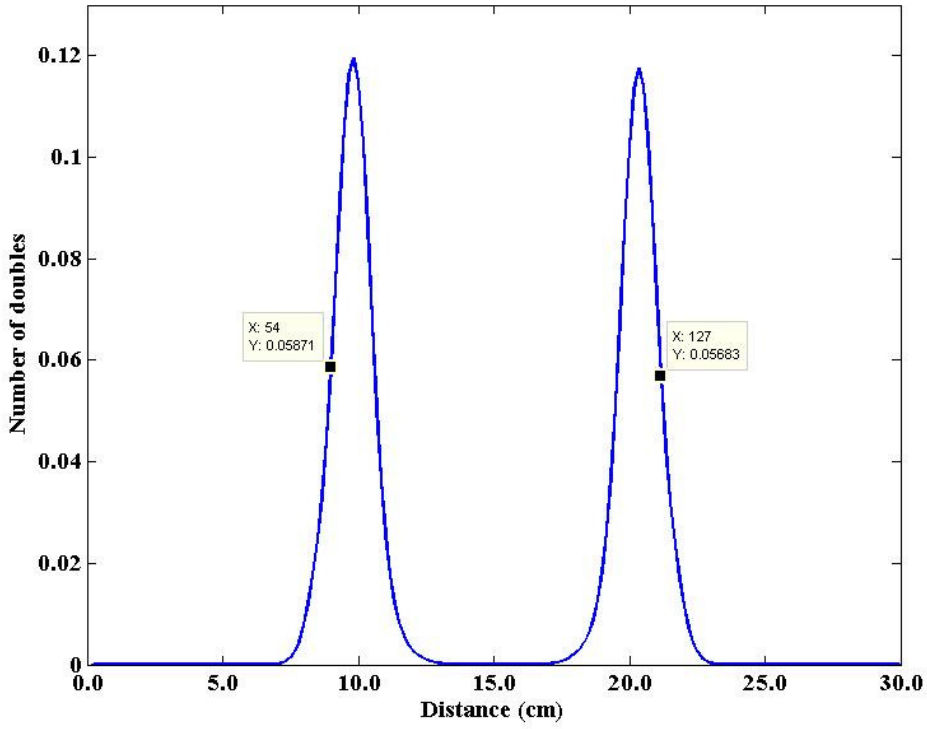

Figure 22. Centerline slice of the MLEM fission reconstruction doubles tomograph with the two peaks corresponding to the cylindrical region of HEU shielded on the outside by a region of DU. This plot was used to determine the radius of HEU in Object 1.

Synthesis of Neutron and Photon Data into an Initial Estimate of Object 1

Synthesis of the gamma and neutron information gathered thus far led to the formation of a guess of the geometry and composition of Object 1, which was which was the basis for a MCNP-PoliMi model. This geometry was constructed as follows: a central void inside of HEU (enrichment unknown), which was inside of DU (0.2 wt% ^{235}U) and polyethylene material regions (Figure 23).

To quantify the unknown enrichment of the HEU region, an interpolation process needed to be conducted. This will be further detailed in the next section, but this process required the creation of four MCNP-PoliMi models were created of varying enrichment: 40, 60, 80, and 93 wt% ^{235}U. The reference time coincidence distribution data could then be compared to that from four models to determine an estimate of the enrichment of the HEU present in Object 1.

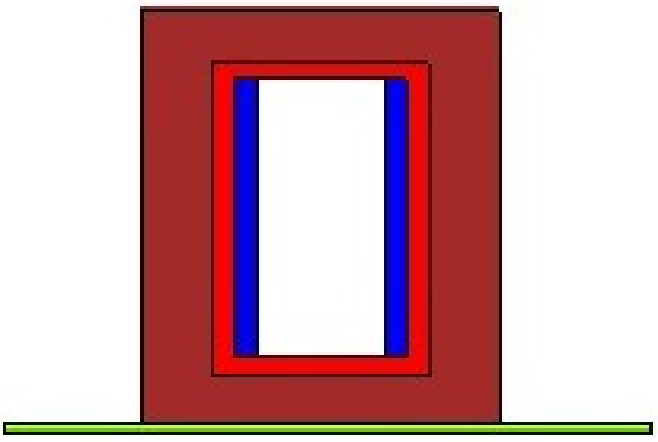

Figure 23. MCNP-PoliMi geometry, with void (white), HEU (blue), DU (red), and polyethylene (dark red) material regions shown. The stainless steel measurement table is also illustrated (green).

Interpolation for HEU Enrichment Determination

Time Distribution of Coincidences between Detectors and Source Pixels

Once the four MCNP-PoliMi models of varying enrichment had been created, the first step in the interpolation process for HEU enrichment determination was to examine the time distribution of coincidences between detectors and source pixels, known as time-of-flight (TOF) distributions. The time distributions of coincidences between the detectors and each source pixel were generated using the singles and doubles from the induced fission radiation detectors. These plots consisted of the sum of the number of all coincidences (over all rotations) versus the time they were detected, with one graph for each of the sixteen detector pixels. For each pixel, the four models of varying enrichment and the reference data were plotted, yielding five curves per figure. An example of such a plot can be seen in Figure 24, which shows the TOF plot from pixel 9 to illustrate this point.

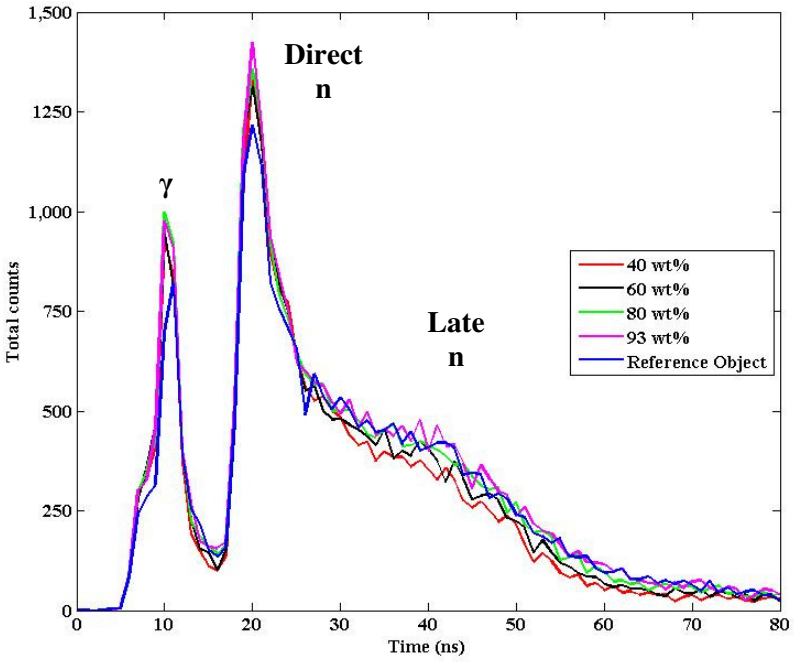

Figure 24. Pixel 9 TOF plot of the total singles counts vs. time for the four MCNP-PoliMi models (red, black, green, and pink) and the reference data (blue). Gamma (γ), and direct and late neutron (n) peaks are labeled.

There are several significant facts that can be obtained from these plots. Photons, produced by inelastic scatter within the object and traveling at the speed of light, arrive much faster than direct neutrons and are detected first (gammas arrive at about 7-10 ns); thus, two distinct peaks are visible in any TOF plot (Figure 24). There is also often a slight rise in counts after the sharp initial neutron peak from "late" neutrons. Its position in time is the result of the time it takes for the source neutrons to reach the HEU and time-of-flight of induced fission radiation to the detectors. Its magnitude is indicative of fission multiplication. For this reason, this region is an indicator of enrichment level, everything else being the same; the higher the counts in this region, the greater the enrichment or fissile mass that is present. It can be seen in the TOF plot in Figure 24 that the "late" neutrons are detected from approximately 35 to 80 ns.

Creation of Enrichment Curves for Interpolation for Enrichment Determination

With TOF plots thus generated for every pixel, enrichment curves could be created for all sixteen pixels, as well. However, as was established earlier with the fission mapping studies, only alpha pixels 5 through 12 were associated with the neutrons incident on the HEU region (Figure 17); therefore, these were the only pixels used for this analysis. The reasoning for this is similar to the logic for integrating between 35 and 80 ns and is derived from the fact that the effects (i.e., neutron scatter instead of fission) of other materials present in Object 1 needed to be limited.

Thus, eight enrichment curves were generated as follows. As was stated previously, each TOF plot had five curves: four for the four MCNP-PoliMi models and one for the reference data (Figure 24). All five were integrated between 35 and 80 ns to obtain the induced fission radiation fission counts resulting from the HEU. The four integrated counts resulting from the four MCNP-PoliMi models of varying enrichment were then plotted against their enrichment in weight percent to produce an enrichment curve for interpolation for enrichment determination for pixels 5 through 12. An example of such a curve can be seen in Figure 25. The uncertainty was taken to be the square root of the counts, and enrichment curves were fit with a second-order polynomial which is detailed in Appendix E.

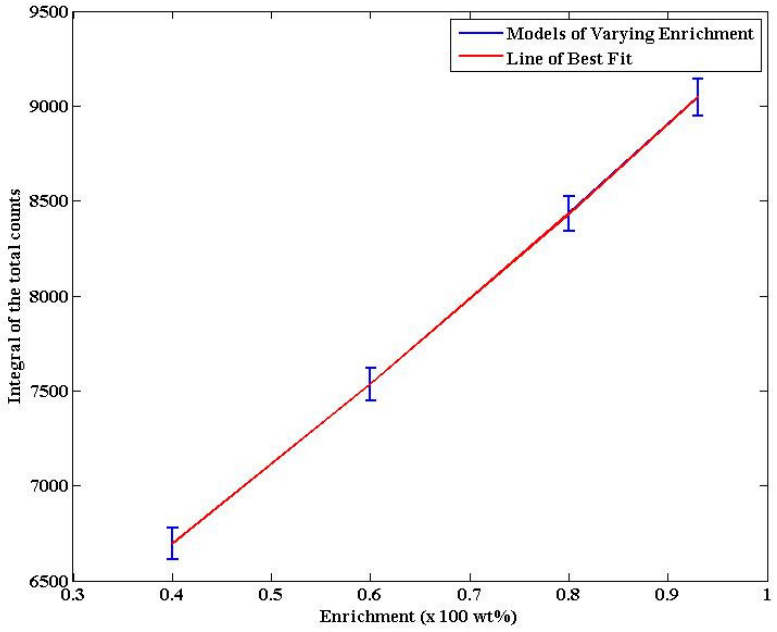

Figure 25. Pixel 9 enrichment curve generated from the integral of the four MCNP-PoliMi models' TOF plots from 35 to 80 ns. Error was taken to be the square root of the counts.

The next step in determining the enrichment of Object 1 was to use the integral of the reference counts to interpolate from the eight enrichment curves. With the integral of the reference data (and therefore a value on the y-axis of the enrichment curve) and the equation of the line of best fit both known, the quadratic formula was used to determine the enrichment. This was equivalent to drawing a horizontal line at a height equal to the integral of the total reference counts from the y-axis to the enrichment curve, and then drawing a vertical line from this intersection point down to the x-axis to determine the enrichment. This is illustrated for pixel 9 in Figure 26, which had an integrated reference counts value of 8783 counts and resulted in an enrichment of 86 wt% ^{235}U.

Upper and lower bounds of enrichment were similarly found for pixels 5 through 12 by using the respective upper and lower endpoints of the error bars, which corresponded to 1σ. Enrichment values for the eight pixels in question, as well as their average values, can be seen in Table 6. It was therefore determined that the average enrichment (averaged over the eight pixels in question) of the HEU present in Object 1 was 84.7 wt% ^{235}U, with 1σ (68.3%) probability of being between 82.8 and 86.6 wt% ^{235}U.

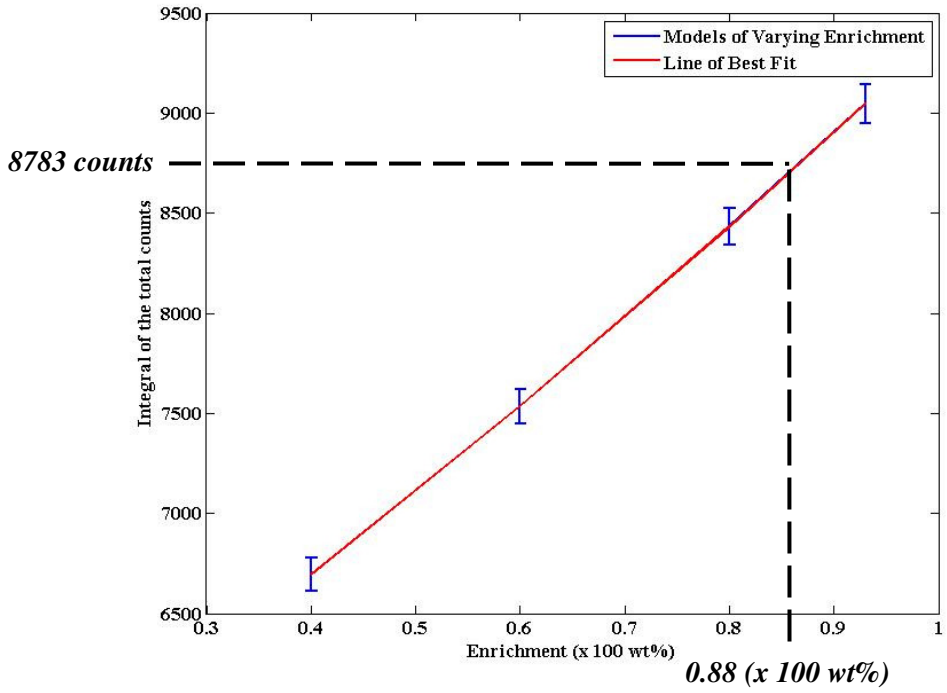

Figure 26. Illustration of the interpolation method equivalent to the quadratic formula used to determine the enrichment of the HEU region of Object 1. Here, the plot and numbers provided are for Pixel 9. Error was taken to be the square root of the counts.

Table 6. Bounds of enrichment (1σ) for pixels 5 through 12 for Object 1

Pixel Number	E_{low} (wt%)	E (wt%)	E_{high} (wt%)
5	78.6	80.9	83.1
6	84.4	86.3	88.3
7	84.1	85.8	87.4
8	85.1	86.7	88.3
9	85.5	87.5	89.5
10	85.4	87.2	89.0
11	81.5	83.1	84.7
12	77.9	80.3	82.6
Average	82.8	84.7	86.6

CHAPTER V
DESCRIPTION OF THE UNKNOWN OBJECT

After the completion of the examination of the simulated neutron and gamma data outlined above, the final estimate of Object 1 was a cylindrical object with the dimensions and material regions listed in Table 7. DU and HEU were 0.2 wt% and 84.7 wt% ^{235}U, respectively. The true geometry of Object 1 was later revealed (also included in Table 7). The mass of ^{235}U was also calculated for the HEU and DU regions for the final estimate and actual geometry (Table 8).

Uncertainty analysis of radial and height dimensions, as well as of the volume of each material region, can be seen in Table 9. Most of the error results from the heights of the components of Object 1, which were derived from the vertical scan. This is because the vertical scan image is less clear than the radial scan. Enrichment estimates (and therefore ^{235}U mass) would have also been more accurate with more accurate radial and height dimensions; enrichment would have decreased to compensate from 84.7 wt% toward the actual enrichment of 80.0 wt% ^{235}U due to multiplication [Ref. 18]. Additional data that could increase the speed and accuracy of geometry analysis are detailed below in Chapter VI.

Table 7. Final estimate and actual geometry of Object 1

	Final Estimate		Actual Geometry	
Material Region	**Radius (cm)**	**Height (cm)**	**Radius (cm)**	**Height (cm)**
Void	4.609	17	4.445	15.24
HEU	6.080	17	6.350	15.24
DU	7.500	19	7.620	17.80
Polyethylene	12.352	25	12.700	25.40

Table 8. Mass of ^{235}U in the final estimate and actual geometry of Object 1

Fissile Material	Final Estimate Mass ^{235}U	Actual Geometry Mass ^{235}U	Percent Error (%)
HEU	13.43 kg	14.89 kg	-9.7
DU	52.29 g	49.76 g	-5.1

Table 9. Percent difference between final estimate and actual geometry of Object 1

Material Region	Radial Percent Error (%)	Height Percent Error (%)
Void	3.69	12
HEU	-4.25	12
DU	-1.58	7
Polyethylene	-2.74	-2

CHAPTER VI
ANALYSIS OF THE ITERATIVE METHODOLOGY

Further Analysis of Auto- and Cross-Correlations

A similar analysis of Object 1 should be performed using the auto- and cross-correlation functions between detectors to determine the enrichment. These functions yield plots similar in shape and meaning to TOF plots in that they have an initial gamma peak followed by a neutron peak that is comprised of direct and late neutrons. However, auto- and cross-correlations plot the time behavior of coincident neutron doubles, whereas TOF plots are for neutron singles. As a result, auto- and cross-correlations may be a better measure of multiplication than TOF plots and therefore may be better at estimating through interpolation the enrichment of the fissile material present in the unknown object.

Fission Mapping Along the Vertical Axis

Another piece of information that should be examined for future use with NMIS measurements and simulations of measurements is fission mapping along the vertical axis. This would have shown that there was DU on the top and bottom of the HEU region, instead of that being assumed. This would alleviate the problem outlined previously that has been encountered with transmission imaging: DU and HEU appear the same in a transmission image due to their similar attenuation coefficients. By mapping fission sites along the vertical axis of an unknown object, this could have been more concretely determined.

Further Analysis of the Method to Determine the Radius of the HEU Region

When determining the HEU-DU boundary from the slice of the doubles MLEM fission reconstruction, it had been assumed that a valid approximation was the halfway point between the maximum amount of doubles (corresponding to HEU) and near zero doubles (corresponding to DU). Further attention should be given to this methodology to optimize it, if possible, and increase accuracy with respect to dimensions and enrichment.

CHAPTER VII
SUMMARY AND CONCLUSIONS

Simulated transmission neutron imaging data, induced fission radiation detector data (MCNP-PoliMi), and passive and active gamma spectroscopy data (MCNPX version 2.6.0) were provided for analysis to determine the geometry and material composition of an unknown object (Object 1). Using a previously determined procedure, the passive gamma spectrum was first analyzed for the presence of fissile material peaks. These peaks were then used to estimate enrichment and compared to the results of GADRAS, a multiple regression iterative analysis code. The active gamma spectrum was then inspected to determine the presence of non-fissile material in Object 1. The results of these two steps were next combined to form a list of possible materials comprising the unknown object: DU and polyethylene.

Next, neutron transmission imaging data was studied. The FBP vertical scan of the object was examined to determine the heights of material regions at which to conduct a radial neutron transmission image. Two radial neutron transmission images of Object 1 were then formed using algorithms which implement the FBP and MLEM iterative reconstruction transmission imaging methods. These images were studied to determine the number of material regions and their material attenuation coefficients (and thus material type, cross-referenced with the list resulting from the gamma spectra). The radii of these material regions were then found using TAKE, an iterative fitting algorithm that determined the dimensions and attenuation coefficients. It was also at this point that it was determined that Object 1 had a cylindrical geometry. To ascertain whether HEU was present and being shielded by an outer region of DU, MLEM fission site reconstruction was employed. Since most of the fissions were occurring inside of the DU metal, this indicated that HEU metal was on the inside.

At this point, an estimate of the geometry of Object 1 was formed: a central void surrounded by HEU of unknown enrichment, nested inside of DU (0.2 wt% ^{235}U), with an outer shell of polyethylene. This geometry was entered into a MCNP-PoliMi model that had four different enrichments of HEU to compare the calculated time distribution of coincidences as a function of enrichment between the induced fission radiation detectors and the alpha pixels to the reference data. Fission mapping also determined which pixels induced fission in the HEU (pixels 5 through 12). The Feynman variance as a function of pixel number was also calculated

for each pixel to corroborate the assumption that pixels 5 through 12 were associated with neutrons that were incident on the HEU region of Object 1.

After integrating these corresponding TOF plots between 35 and 80 ns (the time at which induced fission neutrons reach the fission radiation detectors) and plotting the integral of the counts against the enrichment, the integral of the counts from the reference data was used to interpolate and find a pixel-specific enrichment of the HEU in Object 1. This was then averaged to yield an overall estimate of 84.7 wt% ^{235}U. Statistical uncertainty (taken to be the square root of the counts) was used to find upper (86.6 wt%) and lower (82.8 wt%) bounds of 1σ on this estimate. The actual enrichment was 80 wt%, so the estimate was within 2.5σ of the true value. This estimate could be improved by longer count times which would reduce error.

Comparing the final estimated dimensions to ground truth, error between the estimated and actual geometry varied. Radially, relative error varied from 1.58% to -4.25%, with the greatest error in the HEU region; height-wise, relative error ranged from -2% to 12%. Relative error in the amount of kilograms present of ^{235}U in the HEU was -9.7% which corresponded to an error in the estimate of the enrichment of 5.9 wt%. The bulk of the error was introduced through systematic error introduced by the algorithm which conducted the vertical neutron transmission image reconstruction. These accuracies may be adequate for possible use in future treaty verifications, but the specifics depend on the agreement between treaty partners.

In summary, it is possible to quantitatively determine the materials present and their configuration by iterative analysis using passive and active gamma spectroscopy, FBP and MLEM neutron transmission tomographs (including radial and vertical scans), neutron coincidence and multiplicity counting, and fission mapping data. The unknown object presented here represents a case that is particularly challenging because the fissile material was surrounded by DU. Even so, the region that contains the HEU was identified, and its enrichment was determined within 2.5σ. Therefore, with future work on more complicated material configurations, auto- and cross-correlations, and fission mapping along the vertical axis, it may be possible to reduce uncertainties further and apply this technology to treaty verification.

LIST OF REFERENCES

1. J.T. Mihalczo, J.A. Mullens, J.K. Mattingly, and T.E. Valentine, "Physical description of nuclear materials identification system (NMIS) signatures," *Nuclear Instruments and Methods in Physics Research A*, 450, 531-555 (2000).

2. J.T. Mihalczo, J.K. Mattingly, J.S. Neal, and J.A. Mullens, "NMIS plus gamma spectroscopy for attributes of HEU, PU, and HE detection," *Nuclear Instruments and Methods in Physics Research B*, 213, 378-384 (2004).

3. P.A. Hausladen, P.R. Bingham, J.S. Neal, J.A. Mullens, and J.T. Mihalczo, "Portable fast-neutron radiography with the nuclear materials identification system for fissile material transfers," *Nuclear Instruments and Methods in Physics Research B*, 261, 387-390 (2007).

4. MCNP-PoliMi, http://www-rsicc.ornl.gov/codes/ccc/ccc7/ccc-718.html.

5. MCNPX, http://mcnpx.lanl.gov.

6. J. Mihalczo and J. Mullens, "Nuclear Material Identification System with imaging and gamma-ray spectrometry for plutonium, highly enriched uranium, high explosives, and other materials", Global Nuclear Security Technology Division Report for Oak Ridge National Laboratory, February, 2012.

7. J. Mullens, S. McConchie, P. Hausladen, J. Mihalczo, B. Grogan, and E. Sword, "Neutron radiography and fission mapping measurements of nuclear materials with varying composition and shielding," 52nd Annual INMM Meeting Conference Proceedings, July, 2011.

8. G.F. Knoll, "Radiation Detection and Measurement," 3rd ed., 26-27 (2000).

9. B.R. Grogan, J.T. Mihalczo, S.M. McConchie, and J.A. Mullens, "Identification of shielding material configurations using NMIS imaging," 52nd Annual INMM Meeting Conference Proceedings, July 17, 2011.

10. K. Peña, S. McConchie, J. Crye, and J. Mihalczo, "Active interrogation observables for enrichment determination of DU shielded HEU metal assemblies with limited geometrical information," 52nd Annual INMM Meeting Conference Proceedings, July, 2011.

11. B.R. Grogan and J.T. Mihalczo, "Simulating NMIS imaging and fission-mapping measurements," 52nd Annual INMM Meeting Conference Proceedings, July, 2011.

12. B.R. Grogan, S.M. McConchie, J.T. Mihalczo, and J.A. Mullens, "Alpha detector pixelation effects on NMIS imaging," 49th Annual Meeting of the Institute of Nuclear Materials Management Conference Proceedings, November, 2008.

13. G.W. Phillips, D.J. Nagel, and T. Coffey, “A primer on the detection of nuclear and radiological weapons,” *Center for Technology and National Security Policy, National Defense University* (2005).

14. D. Reilly, N. Ensslin, H. Smith, Jr., and S. Kreiner, “Passive nondestructive assay of nuclear materials,” United States Nuclear Regulatory Commission, March, 1991.

15. GADRAS, http://www-rsicc.ornl.gov/codes/psr/psr5/psr-560.html.

16. R.P. Feynman, D. de Hoffmann, and R. Serber, “Dispersion of the neutron emission in U235 fission”, Report for Los Alamos National Laboratory (1995).

17. S. Fredriksen, “Spatial distribution of induced fission from the pixilated alpha detector in a D-T generator”, Master’s thesis, University of Tennessee-Knoxville, 2009.

18. J. Duderstadt & L. Hamilton, “Nuclear reactor analysis,” Wiley, 84 (1976).

APPENDIX

Appendix A: Process for the Analysis of NMIS Type Neutron Imaging and Gamma Spectroscopy

The procedure for analyzing NMIS type neutron imaging and gamma spectroscopy data is quoted below from Ref. [6], with a flowchart below for ease of visualization (Figure A.1):

1. *Perform passive gamma-ray spectrometry measurements with no object to determine background.*

2. *Perform passive NMIS time correlation measurements with no object to determine background and determine time coincidence distributions and multiplicities.*

3. *Perform baseline I0 measurement with no object with the subsampling that will be used later for the vertical radiographic image scan and the tomographic slice image. (I0 is the neutron flux counted when no target is present, that is, a calibration of the efficiency of the transmission detection system.)*

4. *Perform gamma-ray spectrometry measurements with the sources turned on to obtain the active background from the nearby materials.*

5. *Locate the target object appropriately and measure its location.*

6. *Perform passive gamma-ray spectrometry with object.*

7. *Perform passive time correlation measurements to see if plutonium or HEU is present.*

8. *Evaluate the passive data to make preliminary conclusions including running a GADRAS-like code.*

9. *Perform a shadowgraph (radiograph) imaging scan to determine overall shape of the object and find location of interest for more detailed imaging.*

10. *Perform detailed tomographic slice image measurements at heights of interest to determine the internal configuration. Measure at least two turntable rotary positions if possible.*

11. *Perform time-tagged gamma spectrometry at the same time as step 10 at locations of interest to assist in the identification of materials.*

12. *Reconstruct transmission data using MLEM algorithm. Use resulting images to create the initial guess for dimensions and attenuation coefficients of individual parts inside of the object.*

13. *Run TAKE to determine dimensions and attenuation coefficients of individual parts using information obtained in step 10.*

14. *Reconstruct fission site images from multiplicity singles and doubles data using MLEM algorithm.*

15. *Overlay singles and doubles reconstructions onto transmission reconstructions to identify which internal parts are composed of fissile material.*

16. *Look at the neutron scattering time-of-flight data for each pixel to identify light materials.*

17. *Look at passive and active gamma-ray spectra to determine the presence of and the relative amounts of isotopes of interest in the object. Subtraction of the passive data from the active should give the non-elastic gamma production to identify explosives and other materials.*

18. *Come up with a simple 1-D model using the results from previous steps and fit the model parameters to the passive gamma spectra using GADRAS.*

19. *Develop a MCNP model of the system based on the previous steps.*

20. *Run MCNP simulations of measured quantities (possibly including transmission, fission mapping, neutron scattering, and active gamma spectrometry).*

21. *Generate passive gamma spectrum using the GADRAS 1-D model.*

22. *Compare results of steps 20–21 with measurements and generate a goodness-of-fit value.*

23. *Check on the goodness-of-fit result for convergence. If converged, then end; otherwise, modify model dimensions and materials and return to step 20.*

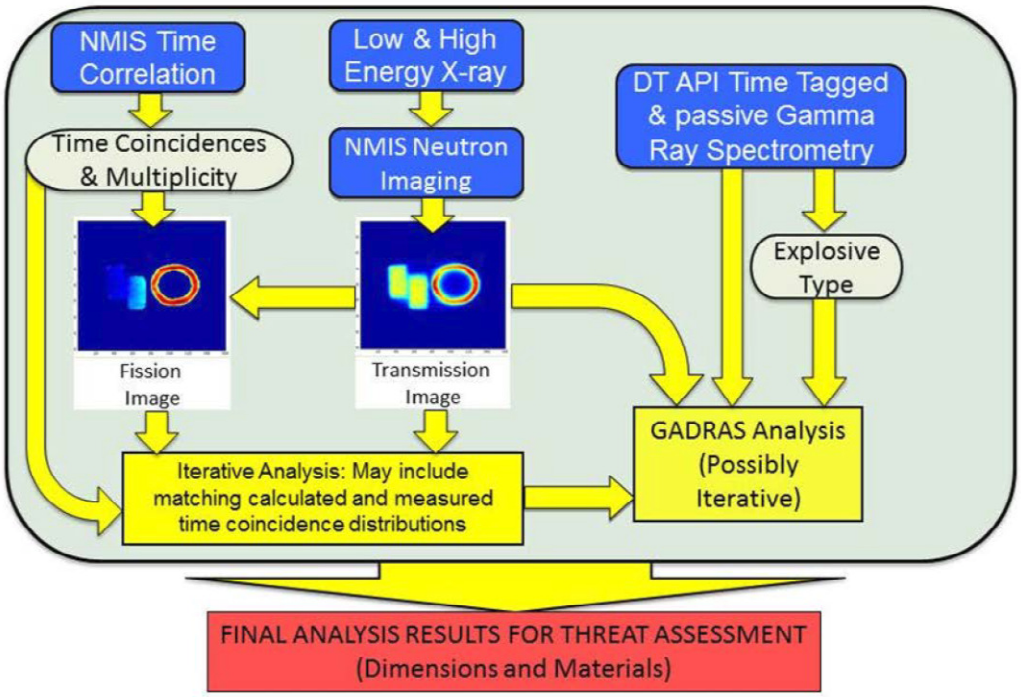

Figure A.1. General flowchart depicting the steps necessary for analyzing NMIS type neutron imaging and gamma spectroscopy data [Ref. 6].

Appendix B: Estimation of Uranium Enrichment from 186-1001 Gamma Lines

The equations below use the following variables, with their values listed in Table B.1:

- t (s) is the live time of the passive gamma spectroscopy measurement
- A_{186}, A_{1001} are the net counts under the 186 keV and 1001 keV peaks, respectively
- $T_{\frac{1}{2},235}, T_{\frac{1}{2},238}$ (s) are the half-lives of ^{235}U and ^{238}U, respectively
- Y_{186}, Y_{1001} are the fraction of decays that produce the 186 keV and 1001 keV peaks, respectively
- N_{235}, N_{238} are the number of ^{235}U and ^{238}U atoms
- E (wt%) is the estimate of the ^{235}U enrichment

Table B.1. 186 and 1001 keV net peak areas, fraction of decays, and half lives for ^{235}U and ^{238}U used to estimate enrichment of Object 1

A_{186}	A_{1001}	Y_{186} (%)	Y_{1001} (%)	$T_{\frac{1}{2},235}$(s)	$T_{\frac{1}{2},238}$(s)	t (s)	E (wt%)
1157	29,724	57.2	0.839	2.22×10^{16}	1.41×10^{17}	900	0.056%

$$N_{235} = \frac{A_{186}}{Y_{186} exp\left(\frac{-ln(2)t}{T_{\frac{1}{2},235}}\right)} \approx \frac{A_{186}}{Y_{186}}$$

$$N_{238} = \frac{A_{1001}}{Y_{1001} exp\left(\frac{-ln(2)t}{T_{\frac{1}{2},238}}\right)} \approx \frac{A_{1001}}{Y_{1001}}$$

$$E(wt\%) = \frac{235(N_{235})}{235(N_{235}) + 238(N_{238})}$$

Appendix C: Estimation of Uranium Enrichment from 186-258 Gamma Lines

The equations below use the following variables, with their values listed in Table C.1:

- t (s) is the live time of the passive gamma spectroscopy measurement
- A_{186}, A_{258} are the net counts under the 186 keV and 258 keV peaks, respectively
- $T_{\frac{1}{2},235}, T_{\frac{1}{2},238}$ (s) are the half-lives of ^{235}U and ^{238}U, respectively
- Y_{186}, Y_{258} are the fraction of decays that produce the 186 keV and 258 keV peaks, respectively
- N_{235}, N_{238} are the number of ^{235}U and ^{238}U atoms
- E (wt%) is the estimate of the ^{235}U enrichment

Table C.1. 186 and 258 keV net peak areas, fraction of decays, and half lives for ^{235}U and ^{238}U used to estimate enrichment of Object 1

A_{186}	A_{258}	Y_{186} (%)	Y_{258} (%)	$T_{\frac{1}{2},235}$(s)	$T_{\frac{1}{2},238}$(s)	t (s)	E (wt%)
1157	2110	57.2	7.3×10^{-2}	2.22×10^{16}	1.41×10^{17}	900	0.066%

$$N_{235} = \frac{A_{186}}{Y_{186} exp\left(\frac{-ln(2)t}{T_{\frac{1}{2},235}}\right)} \approx \frac{A_{186}}{Y_{186}}$$

$$N_{238} = \frac{A_{258}}{Y_{258} exp\left(\frac{-ln(2)t}{T_{\frac{1}{2},238}}\right)} \approx \frac{A_{258}}{Y_{258}}$$

$$E(wt\%) = \frac{235(N_{235})}{235(N_{235}) + 238(N_{238})}$$

Appendix D: Derivation of Feynman Variance

The equations below use the following variables:

- m_1, m_2 are the measured singles and doubles counts, respectively
- y_1, y_2 are the singles and doubles with random counts removed, respectively
- $Y(T)$ is the Feynman variance

Please note the following definitions that are used in the derivation:

- $\binom{n}{k} = \frac{n!}{k!(n-k)!}$
- $Y(T) = \left(\frac{\overline{c^2} - \bar{c}^2}{\bar{c}} - 1\right)$

$$y_1 = m_1 = \sum_{j=1}^{3} \binom{j}{1} b_j = \sum_{j=1}^{3} j\, b_j = \bar{c}$$

$$y_2 = m_2 - \frac{{y_1}^2}{2!} = \sum_{j=2}^{3} \binom{j}{2} b_j - \frac{{y_1}^2}{2} = \sum_{j=2}^{3} \binom{j}{2} b_j - \frac{\left(\sum_{j=1}^{3} j\, b_j\right)^2}{2}$$

$$y_2 = \sum_{j=2}^{3} \frac{j(j-1) b_j}{2} - \frac{\left(\sum_{j=1}^{3} j\, b_j\right)^2}{2} = \frac{1}{2}\left(\sum_{j=2}^{3} j^2 b_j - \sum_{j=1}^{3} j b_j - \left(\sum_{j=1}^{3} j b_j\right)^2\right)$$

$$y_2 = \frac{1}{2}\left(\overline{c^2} - \bar{c}^2 - \bar{c}\right)$$

$$\frac{y_2}{y_1} = \frac{1}{2}\left(\frac{\overline{c^2} - c^2}{\bar{c}} - 1\right) = \frac{1}{2} Y(T)$$

$$\therefore Y(T) = 2\left(\frac{y_2}{y_1}\right)$$

Appendix E: Enrichment Curve Fit Values

The line of best fit equation used to form the enrichment curves to determine the enrichment of the HEU present in Object 1 employs the following variables, with their values listed in Table E.1:

- $N_{integrated}$ is the number of integrated reference counts on the TOF plots of pixels 5 through 12 over the window of 35 to 80 ns
- E (wt%) is the estimate of the ^{235}U enrichment
- a, b, and c are constants determined by Matlab to best fit the plotted data

---

Table E.1. Integrated reference counts, $N_{integrated}$, and line of best fit constants, a, b, and c, used to interpolate to determine the enrichment, E, of the HEU in Object 1

Pixel Number	$N_{integrated}$	a	b	c
5	7463	98.81	-77.09	1220.84
6	8948	-136.90	491.89	2448.59
7	8957	-21.27	807.05	3644.96
8	8861	1480.86	-504.12	4926.66
9	8783	1350.36	1644.52	5248.53
10	8944	1366.58	2523.02	5750.99
11	8819	2912.10	898.96	6043.78
12	7316	3010.97	771.00	5928.31

$$N_{integrated} = aE^2 + bE + c$$

VITA

Alicia Swift received her Bachelor's of Science in nuclear engineering and minor in physics from the University of Florida in 2010. While there, she constructed computer models of nuclear reactors and conducted port security experiments on the detection of fissile material in shipping containers. Currently, Alicia is a graduate research assistant in the Department of Nuclear Engineering at the University of Tennessee-Knoxville and is conducting her research at Oak Ridge National Laboratory (ORNL) in the Global Nuclear Security Technology Division (GNSTD). Alicia's Master's thesis research is concentrated on the development and application of nonproliferation and treaty enforcement technologies. Alicia will graduate with a Master's of Science in May, 2012 with a certificate in Nuclear Security Science and Analysis. Her future academic career goals include the completion of the year-long Nonproliferation Graduate Fellowship Program (NGFP) with the National Nuclear Security Administration (NNSA), followed by a return to the University of Tennessee-Knoxville to finish her PhD studies in nuclear engineering.